Article

Cell Reports

Genome-wide Integrative Analysis of Zika-Virus-Infected Neuronal Stem Cells Reveals Roles for MicroRNAs in Cell Cycle and Stemness

Graphical Abstract

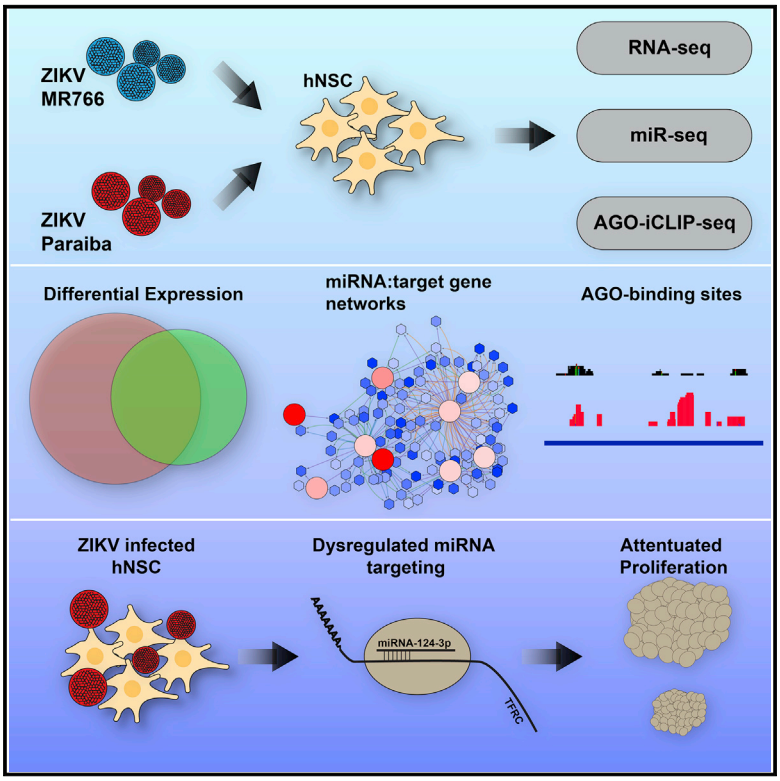

Authors

Jason W. Dang, Shashi Kant Tiwari, Yue Qin, Tariq M. Rana

Correspondence

trana@ucsd.edu

In Brief

Dang et al. investigate the dysregulation of miRNAs in Zika-virus-infected neural stem cells and identify miR-124-3p as a potential regulator of Zika-virus-mediated microcephaly.

Highlights

- Transcriptomic profiling identified dysregulated miRNAs in ZIKV-infected stem cells
- miRNAs regulate the cell cycle, stem cell maintenance, and neurogenesis pathways
- *miR-124-3p* regulates expression of transferrin receptor (*TFRC*) mRNA

Dang et al., 2019, Cell Reports *27*, 3618–3628
June 18, 2019
https://doi.org/10.1016/j.celrep.2019.05.059

CellPress

OPEN ACCESS
CellPress

Cell Reports
Article

Genome-wide Integrative Analysis of Zika-Virus-Infected Neuronal Stem Cells Reveals Roles for MicroRNAs in Cell Cycle and Stemness

Jason W. Dang,[1,2,3] Shashi Kant Tiwari,[1,2] Yue Qin,[1,2,4] and Tariq M. Rana[1,2,5,6,7,8,*]
[1]Department of Pediatrics, University of California, San Diego, 9500 Gilman Drive, MC 0762, La Jolla, CA 92093, USA
[2]Division of Genetics, University of California, San Diego, 9500 Gilman Drive, MC 0762, La Jolla, CA 92093, USA
[3]Department of Bioengineering, University of California, San Diego, 9500 Gilman Drive, MC 0412, La Jolla, CA 92093, USA
[4]Bioinformatics and Systems Biology, University of California, San Diego, 9500 Gilman Drive, MC 0419, La Jolla, CA 92093, USA
[5]Program in Immunology, University of California, San Diego, 9500 Gilman Drive, MC 0762, La Jolla, CA 92093, USA
[6]Institute for Genomic Medicine, University of California, San Diego, 9500 Gilman Drive, MC 0762, La Jolla, CA 92093, USA
[7]Moores Cancer Center, University of California, San Diego, 9500 Gilman Drive, MC 0762, La Jolla, CA 92093, USA
[8]Lead Contact
*Correspondence: trana@ucsd.edu
https://doi.org/10.1016/j.celrep.2019.05.059

SUMMARY

Zika virus (ZIKV) infection is implicated in severe fetal developmental disorders, including microcephaly. MicroRNAs (miRNAs) post-transcriptionally regulate numerous processes associated with viral infection and neurodegeneration, but their contribution to ZIKV pathogenesis is unclear. We analyzed the mRNA and miRNA transcriptomes of human neuronal stem cells (hNSCs) during infection with ZIKV MR766 and Paraiba strains. Integration of the miRNA and mRNA expression data into regulatory interaction networks showed that ZIKV infection resulted in miRNA-mediated repression of genes regulating the cell cycle, stem cell maintenance, and neurogenesis. Bioinformatics analysis of Argonaute-bound RNAs in ZIKV-infected hNSCs identified a number of miRNAs with predicted involvement in microcephaly, including *miR-124-3p*, which dysregulates NSC maintenance through repression of the transferrin receptor (*TFRC*). Consistent with this, ZIKV infection upregulated *miR-124-3p* and downregulated *TFRC* mRNA in ZIKV-infected hNSCs and mouse brain tissue. These data provide insights into the roles of miRNAs in ZIKV pathogenesis, particularly the microcephaly phenotype.

INTRODUCTION

Zika virus (ZIKV) is a re-emerging arbovirus belonging to the Flaviviridae family and has recently been linked to severe fetal abnormalities, including microcephaly and fetal growth restriction (Brasil et al., 2016; Lazear and Diamond, 2016; Sarno et al., 2016). *In vitro* and *in vivo* studies have shown that ZIKV preferentially infects neuronal stem and/or progenitor cells and immature neurons in the developing brain and dysregulates processes involved in cell-cycle progression, differentiation, apoptosis, autophagy, and immune activation (Cugola et al., 2016; Dang et al., 2016; Li et al., 2016a, 2016b; Liang et al., 2016; Tang et al., 2016). However, the molecular mechanisms by which ZIKV perturbs the transcriptomic landscape or leads to microcephaly are not well understood.

MicroRNAs (miRNAs) are a class of small non-coding RNAs (~22 nt in length) that play critical roles in regulating protein expression. miRNAs act post-transcriptionally by binding to partially complementary sites in the 3′ UTR of target mRNAs. This sequence-specific interaction leads to translational repression or mRNA degradation through Argonaute proteins within the RNA-induced silencing complex (RISC), which cleave the mRNA and recruit other proteins that repress translation or promote degradation. The mRNA targeting specificity of miRNAs is controlled by many factors, including base pairing between the miRNA 5′ seed sequence and mRNA 3′-UTR sequence, cooperativity between multiple miRNA-binding sites, and the position of miRNA-binding sites in the targeted mRNA (Agarwal et al., 2015; Ambros, 2004; Bartel, 2009; Cloney, 2016; Grimson et al., 2007; Lewis et al., 2005; Pasquinelli, 2012). This flexibility means that individual miRNAs are capable of repressing the translation of hundreds of target mRNAs (Baek et al., 2008; Selbach et al., 2008). As a result, miRNAs are known to play pivotal roles in the post-transcriptional regulation of numerous biological processes.

Little is currently known about the role of miRNAs in ZIKV pathogenesis and microcephaly. Given their documented roles in regulating neurodegeneration, viral infection, and innate immunity (Eacker et al., 2009; Lanford et al., 2010; Liu et al., 2012; O'Connell et al., 2010; Sullivan and Ganem, 2005; Taganov et al., 2006; Wang et al., 2006), we hypothesized that miRNAs may play a significant role in ZIKV pathogenesis, particularly the effects on the developing brain. Here, we report that ZIKV infection dysregulates both coding gene and miRNA transcriptomes of human neuronal stem cells (hNSCs). We performed meta-analyses and constructed regulatory interaction networks to integrate the miRNA and mRNA expression data, with the goal of shedding light on the potential role of miRNA-mediated target

gene repression during ZIKV infection. We identified a number of miRNAs, including *let-7c* and *miR-124-3p*, that mediate the suppression of gene networks involved in cell-cycle progression and stem cell maintenance. Collectively, our data provide insight into the function of miRNA-regulated networks in ZIKV-induced pathogenesis, particularly as it pertains to microcephaly.

RESULTS

ZIKV MR766 and Paraiba Modulate the mRNA Transcriptome of hNSCs

To investigate the role of miRNAs during ZIKV pathogenesis, we performed next-generation sequencing of RNA isolated from hNSCs infected with ZIKV strains MR766 (African origin) and Paraiba (Brazilian origin) for 3 days (Figure 1A). Consistent with previous studies showing that ZIKV strains show differences in rates of viral replication (Cugola et al., 2016; Simonin et al., 2016), we found ~10-fold higher levels of infection with MR766 than with Paraiba on the first 3 days after inoculation of hNSCs at the same MOI of 1, as demonstrated by qRT-PCR analysis of ZIKV RNA (Figure 1B). Immunostaining of ZIKV envelope protein (ZIKVE) (Figure 1C) further confirmed higher rates of infection, with MR766 infecting approximately 70% of cells and Paraiba infecting ~30% after 3 days post-inoculation. In addition, we confirmed that ZIKV MR766 produces ~6-fold more infectious viral particles than does ZIKV Paraiba in plaque-forming assays (Figure S1A).

The Paraiba strain had a less significant impact on gene expression in hNSCs, suggesting an overall lower rate of infection as previously indicated (Figures 1B and 1D; Tables S1 and S2). ZIKV MR766 significantly upregulated 1,159 genes and downregulated 1,120 genes (Figures 1D and 1E), compared with only 112 and 178 genes that were significantly upregulated and downregulated, respectively, in ZIKV Paraiba-infected hNSCs (Figures 1D and 1F). In addition, we identified a total of 52 and 52 genes that were commonly upregulated and downregulated, respectively, in both MR766- and Paraiba-infected cells (Figure 1D).

We next performed gene set enrichment analysis (GSEA) of the differentially expressed genes. In MR766-infected hNSCs, the upregulated genes were enriched in functions related to chromosome organization and cell-cycle processes (Figure S1B), whereas the downregulated genes were involved in gene expression, biosynthetic processes, and cell death (Figure S1C). The processes most affected by MR766 infection were those governing chromosome organization, metabolism, cell cycle, and cell stress (Figure S1D), which is consistent with previous reports (Tang et al., 2016). In contrast, the upregulated and downregulated genes in Paraiba-infected hNSCs were all largely related to metabolism and biosynthetic processes, with additional enrichment of genes involved in tissue development and neurogenesis (Figures S1E–S1G).

We considered that the transcriptomic differences induced by ZIKV MR766 and Paraiba might be a consequence of their differing infection rates. Therefore, we infected hNSCs with MR766 at an MOI of 1 for 2 days or with Paraiba at MOIs of 1 or 3 for 2 or 4 days. We then analyzed the top 20 most differentially expressed genes between both strains to assess their similarity as a function of MOI and time point (Figure 1G). Indeed, we found that the Paraiba- and MR766-induced differential gene expression profiles became increasingly similar as the Paraiba MOI and time post-infection increased, indicating that the differential pattern of gene expression was a reflection of the infection level rather than the strain *per se*.

Collectively, these findings indicate that ZIKV MR766 infection and Paraiba infection of hNSCs cause dysregulation of a number of pathways involved in neurogenesis, suggesting that they may contribute to the microcephaly phenotype.

miRNAs Regulate Processes Implicated in ZIKV-Induced Microcephaly

Because miRNAs are potent post-transcriptional regulators, we examined their contribution to the changes in the transcriptome of ZIKV-infected hNSCs. We profiled differential miRNA expression at 3 days post-infection by microRNA sequencing (miRNA-seq) (Figures 2A–2C; Table S3). Although ZIKV MR766 induced a more robust change in the mRNA transcriptome than did Paraiba infection (as described earlier), ZIKV Paraiba induced a significantly greater change in miRNAs, in terms of both quantity and magnitude, likely due to the differing rates of viral replication within neural stem cells. Interestingly, we observed more differentially expressed mRNAs during MR766 viral infection but fewer differentially expressed miRNAs.

To understand the potential mechanistic roles of miRNAs in ZIKV infection and the associated neurodegenerative pathology, we utilized the predictive algorithms TargetScan (Agarwal et al., 2015), miRANDA (Betel et al., 2008), and miRTarBase (Chou et al., 2016) to identify putative mRNA targets of the differentially expressed miRNAs. These algorithms evaluate target seed sequence pairing, site numbers, conservation, and site context scores to predict targets with high confidence. To identify miRNA-mRNA interactions that may be regulated by ZIKV infection, we then cross-checked the list of putative mRNA targets with the mRNAs shown to be most significantly altered by ZIKV infection of hNSCs. GSEA of the dataset indicated that mRNAs satisfying both criteria (i.e., directly modulated by ZIKV infection and putative targets of differentially expressed miRNAs) were enriched in functions related to transcriptional regulation, metabolism, cellular stress response, cell cycle, tissue development, neurogenesis and nervous system development, cell death, and neuron differentiation (Figure 2D). Using qRT-PCR, we validated these data by confirming that ZIKV infection downregulates *NESTIN* and *PAX6* expression, both of which are involved in NSC maintenance (Figure S2A). Similarly, analysis of the datasets from ZIKV Paraiba-infected cells also identified mRNAs likely to be involved in processes related to metabolism, tissue development, neurogenesis, and neuron differentiation (Figure 2E). These data indicate that pathways potentially involved in neurodegeneration feature prominently among the host miRNA-mRNA networks dysregulated by infection of hNSCs with both ZIKV MR766 and Paraiba.

To more precisely map the miRNA-regulated pathways that may contribute to ZIKV pathogenesis, we constructed integrative networks of the ZIKV-modulated miRNAs and miRNA-regulated mRNAs. Genes that were downregulated by ZIKV infection and enriched in gene ontology (GO) functions related to "cell

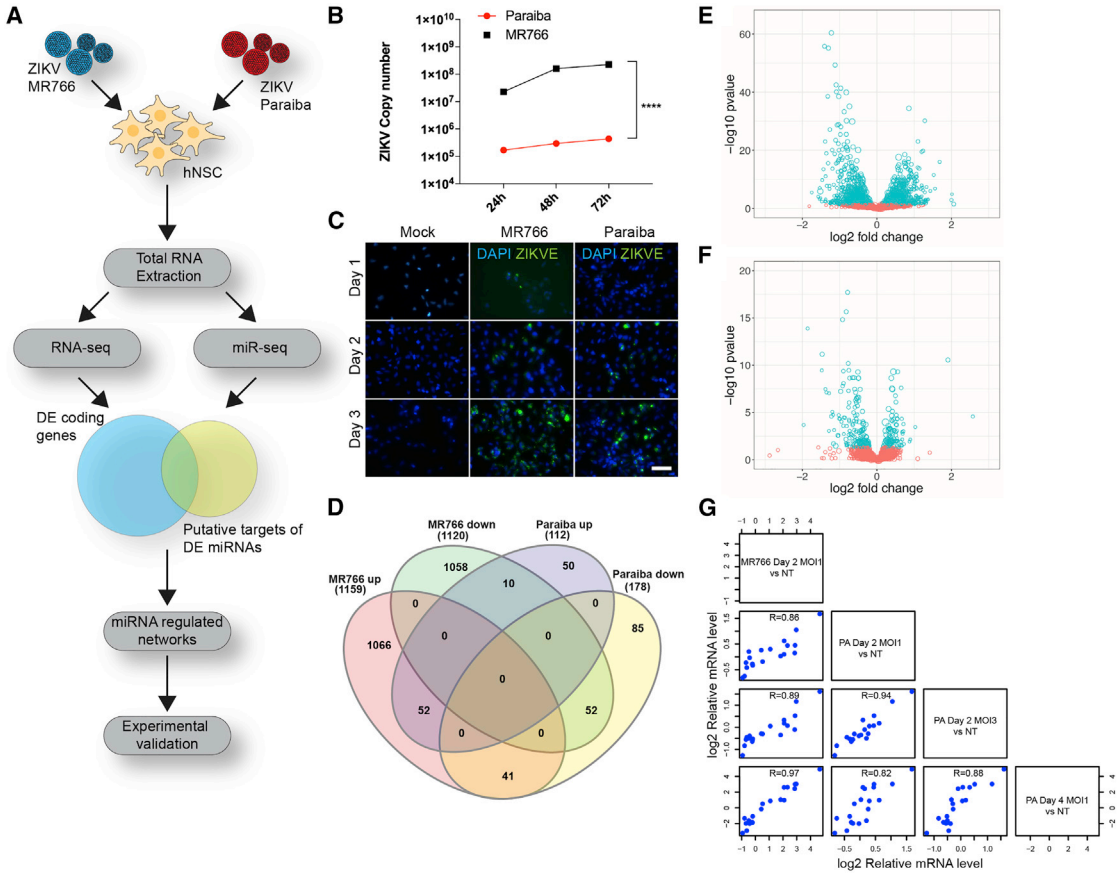

Figure 1. Genome-wide Integrative Analysis of miRNAs in ZIKV-Infected hNSCs

(A) Experimental design. hNSCs were infected with ZIKV MR766 or Paraiba for 3 days at an MOI of 1. Total RNA was analyzed by RNA-seq or miRNA-seq to identify miRNA-regulated networks of genes implicated in ZIKV pathogenesis. DE, differentially expressed.

(B) qRT-PCR analysis of ZIKV MR766 and ZIKV Paraiba copy number on days 1, 2, and 3 post-inoculation of hNSCs at an MOI of 1. Data are means ± SEM of biological triplicates.

(C) Fluorescence immunostaining of ZIKV envelope protein (ZIKVE) in hNSCs on days 1, 2, and 3 post-infection with ZIKV MR766 or Paraiba at an MOI of 1. Nuclei were stained with DAPI. Scale bar, 100 μm.

(D) Venn diagram of differentially expressed genes in ZIKV MR766- and Paraiba-infected hNSCs at 3 days post-infection at an MOI of 1. Up, upregulated; down, downregulated.

(E and F) Volcano plots of the differentially expressed coding genes in (E) MR766-infected and (F) Paraiba-infected hNSCs at 3 days post-infection at an MOI of 1. Blue circles represent significantly (adjusted $p < 0.05$) differentially expressed genes. The size of each circle is proportional to the square root of the base mean expression of the gene.

(G) Scatterplot matrix comparing the relative gene expression of 20 top differentially expressed genes in ZIKV MR766- and Paraiba-infected hNSCs under varying MOIs and time points. Plots show the correlation between differentially expressed genes in MR766- versus Paraiba-infected neural stem cells infected under 4 conditions: with MR766 at an MOI of 1 and analyzed 2 days post-infection; with Paraiba at an MOI of 1 and analyzed 2 or 4 days post-infection; or with Paraiba at an MOI of 3 and analyzed 2 days post-infection. Points represent the mean relative expression level of 20 top differentially expressed genes relative to mock-infected cells in each condition. n = 6 biological replicates.

See also Figure S1.

cycle'' and ''G1/S transition,'' ''defense response to virus,'' and ''brain development'' (Figure 2F, blue hexagons) were cross-referenced with potential miRNA regulators concomitantly upregulated upon ZIKV infection (Figure 2F, red circles). Likewise, genes that were upregulated by ZIKV infection and enriched in ''viral process,'' ''apoptosis,'' ''NF-κB (nuclear factor κB) signaling,'' and ''cell cycle arrest'' were cross-referenced with potential miRNA regulators concomitantly downregulated by ZIKV infection (Figure S2B). These networks indicate that some differentially expressed mRNAs—such as *TP53* or *CDK6*—may be derepressed, and thereby upregulated following infection, due to the downregulation of multiple putative miRNAs. The miRNAs identified from these analyses included many with functions relevant to the pathogenic ZIKV phenotype, including G1/S transition, defense response to virus, brain development (Figure 2F), viral process, apoptosis, NF-κB signaling, and cell-cycle arrest (Figure S2B). We also generated networks of miRNA targets downregulated by ZIKV (Figure S2C) and grouped them by their GO function (Figure S2D). With these analyses, we observed downregulated genes involved in biological

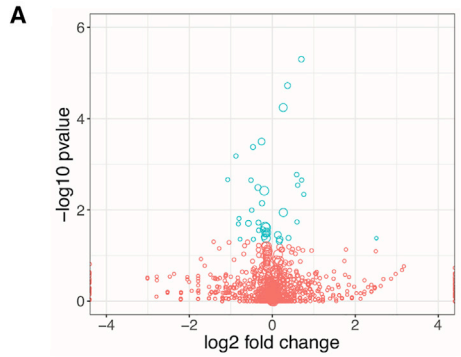

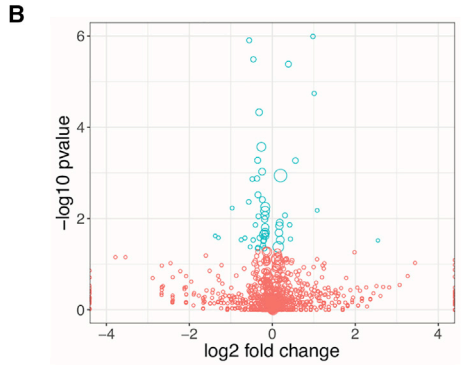

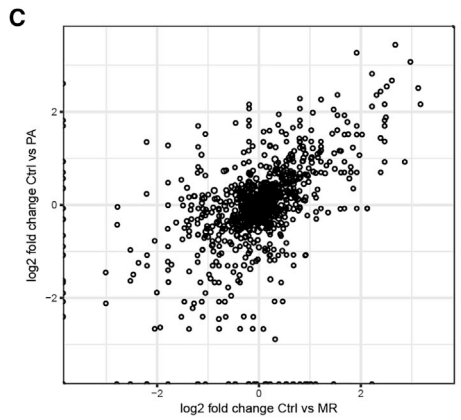

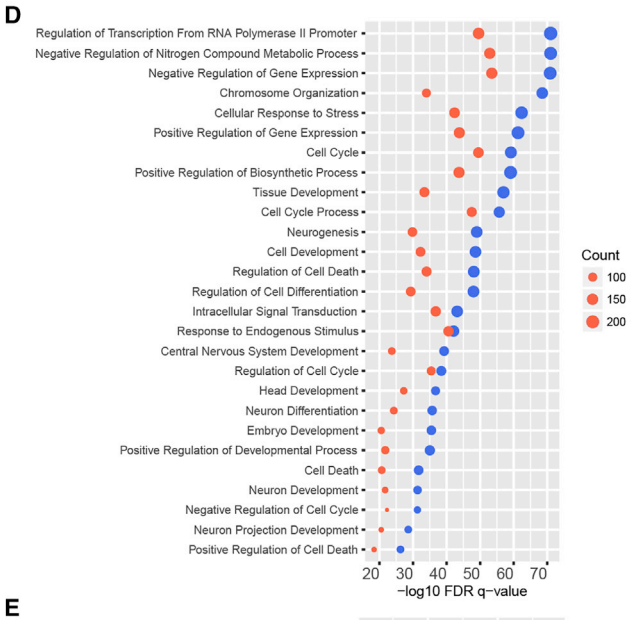

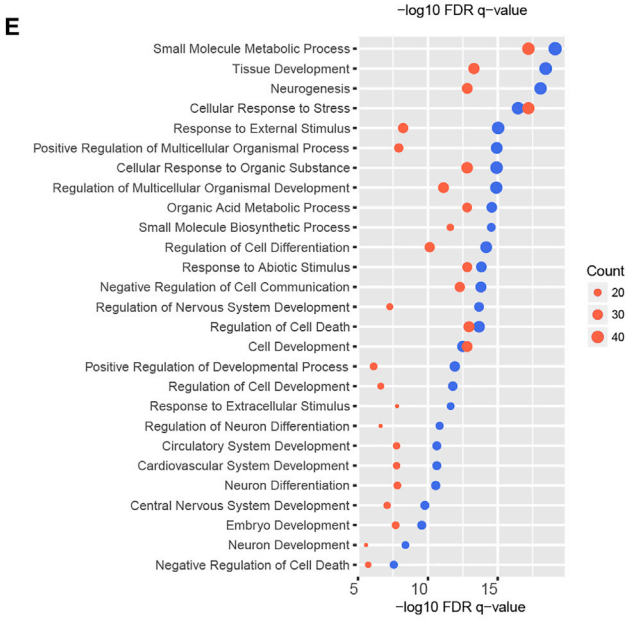

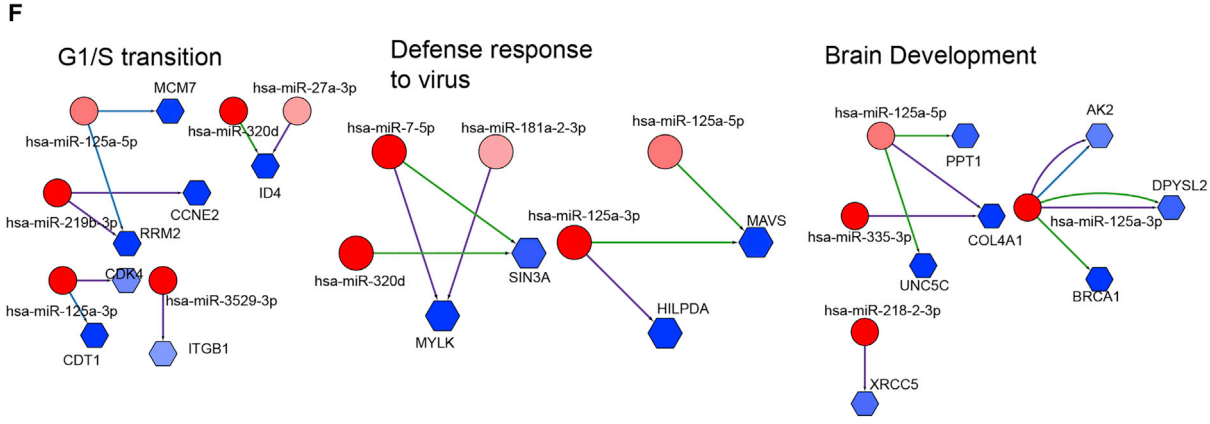

(legend on next page)

processes, including nervous system development, cell-cycle transition, and DNA damage repair. Collectively, these interaction networks identify a number of miRNAs and mRNAs perturbed during ZIKV infection. Further studies including gain and loss of function should be performed to assess the ability of ZIKV to dysregulate multiple miRNAs with effects on the same target mRNA (Figure 2F).

AGO-iCLIP-Seq Identifies Dysregulated miRNA-mRNA Interactions in ZIKV-Infected hNSCs

miRNAs contribute to post-transcriptional regulation of gene expression by associating with Argonaute proteins (AGOs) to repress target gene expression through either mRNA degradation or translational repression within the RISC. Differential expression of miRNAs during viral infection may hint at an important role in viral pathogenesis; however, it does not necessarily indicate a biological function. Thus, to further elucidate the role of miRNA-mRNA networks in ZIKV infection of hNSCs, we performed Argonaute crosslinking and immunoprecipitation followed by sequencing (AGO-iCLIP-seq), which identifies miRNAs and mRNAs bound to AGOs within the RISC (Chi et al., 2009; Haecker et al., 2012; Hafner et al., 2010; König et al., 2010, 2011). To accomplish this, neural stem cells were infected with Paraiba isolates at MOI 1 for 4 days to achieve higher viral titers without significant cell loss and UV crosslinked to covalently bind RNA-protein complexes. Lysates were treated with RNase T1 and immunoprecipitated with a pan-AGO-specific monoclonal antibody to identify all miRNAs and target mRNAs within the RISC following stringent high salt washes. Libraries were generated and sequenced to identify miRNAs and target mRNAs with single-nucleotide resolution. Moreover, AGO-iCLIP-seq may identify biologically significant miRNAs whose expression levels are not changed during viral infection but show greater loading in the RISC or have non-canonical binding sites outside of the 3′ UTR. Furthermore, miRNAs may post-transcriptionally regulate gene expression through various processes, including mRNA degradation and translational repression, both pathways of which are mediated though the association with RISC and AGO. Thus, through analyzing RNAs bound by AGO using AGO-iCLIP-seq, we can address both mRNA degradation and translational repression, which may not necessarily be reflected in RNA-sequencing (RNA-seq) data.

As expected, AGO-associated material from cells was enriched in putative miRNA-binding sites within mRNA 3′ UTRs rather than 5′ UTRs or the coding region of a gene (CDS) of cellular mRNAs (Figure S3A). Interestingly, in ZIKV-infected neural stem cells, we identified many sequences bound to AGO throughout the ZIKV genome (Figure 3A), suggesting that ZIKV gene expression is regulated by host miRNAs. Further experiments should be performed to determine the possible role of miRNAs in targeting viral UTRs as an antiviral host response during ZIKV infection. ZIKV is known to dysregulate many host pathways at the RNA and protein levels, including autophagy via AKT/mTOR signaling (Liang et al., 2016), mitosis (Onorati et al., 2016), and splicing (Hu et al., 2017); thus, we did not observe a clear correlation between ZIKV-induced miRNA expression, mRNA target expression, and AGO binding at a transcriptome level. However, there are cases in which miRNA-seq and AGO-iCLIP-seq data are correlated. For example, the miRNA-seq results indicate that miR-1246 and miR-335 are both upregulated during ZIKV infection and show enhanced binding to AGO (Figures S3B and S3C). Conversely, expression of miR-129-2 and miR-139 was decreased following ZIKV Paraiba infection, which is consistent with their attenuated binding to AGO (Figures S3D and S3E).

Because ZIKV is able to dysregulate many different pathways, we wanted to identify miRNAs specifically targeting genes relevant to microcephaly by repressing host gene expression. For this, the miRNA-seq and AGO datasets were screened against the Harmonizome database (Rouillard et al., 2016), which ranks miRNAs using an aggregate score based on putative target genes associated with microcephaly, curated from the Comparative Toxicogenomics Database (Davis et al., 2017). This analysis identified a number of miRNAs potentially regulating genes significant to microcephaly, from which we selected two, *hsa-let-7c* and *miR-124-3p*, for more detailed investigation (Figure 3B).

We first analyzed the potential role of *let*-7c in ZIKV pathogenesis because of its well-known role in regulating stem cell self-renewal (Büssing et al., 2008; Melton et al., 2010). We confirmed that ZIKV infection did, indeed, upregulate let-7c expression (Figure 3C) and AGO binding (Figure 3D), although this change was only significant for ZIKV Paraiba-infected cells under the conditions used here. Since the let-7c target gene high-mobility group AT-hook 2 (HMGA2) has previously been shown to govern self-renewal of NSCs (Nishino et al., 2008), we analyzed *HMGA2* expression and binding of AGO to the *HMGA2* 3′ UTR following ZIKV infection. Consistent with previous data (Yu et al., 2015) and TargetScan predictions, we observed increased AGO binding to sequences in the *HMGA2* 3′ UTR (Figure 3E) and downregulation of *HMGA2* mRNA levels (Figure 3F) upon ZIKV infection. These data, therefore, suggest that ZIKV induces

Figure 2. Relationship between Differentially Expressed miRNAs and Putative mRNA Targets in ZIKV-Infected hNSCs

(A and B) Volcano plots of differentially expressed miRNAs in (A) MR766- and (B) Paraiba-infected hNSCs at 3 days post-infection. Blue circles represent significantly (adjusted $p < 0.05$) differentially expressed miRNAs. The size of each circle is proportional to the square root of the base mean expression of the gene.

(C) Comparative dot plot of differentially expressed miRNAs in MR766 (MR)- and Paraiba (PA)-infected hNSCs. The size of each circle is proportional to the square root of the base mean expression of the gene.

(D and E) Gene set enrichment analyses (GSEAs) of putative miRNA targets differentially expressed in hNSCs during MR766 (D) and Paraiba (E) infection. Blue represents downregulated mRNAs targeted by upregulated miRNAs; red represents upregulated mRNAs targeted by downregulated miRNAs. The size of the dot is proportional to the number of genes in that enriched GSEA biological category.

(F) Integrative regulatory network analyses showing upregulated miRNAs (red circles) targeting downregulated putative mRNA targets (blue hexagons) based on TargetScan, miRANDA, and miRTarBase. The number of edges between miRNAs and mRNAs is equal to the number of algorithms predicting the miR-mRNA interaction. The blue or red color intensity is proportional to the fold change in expression during ZIKV infection (darker represents larger change).

See also Figure S2.

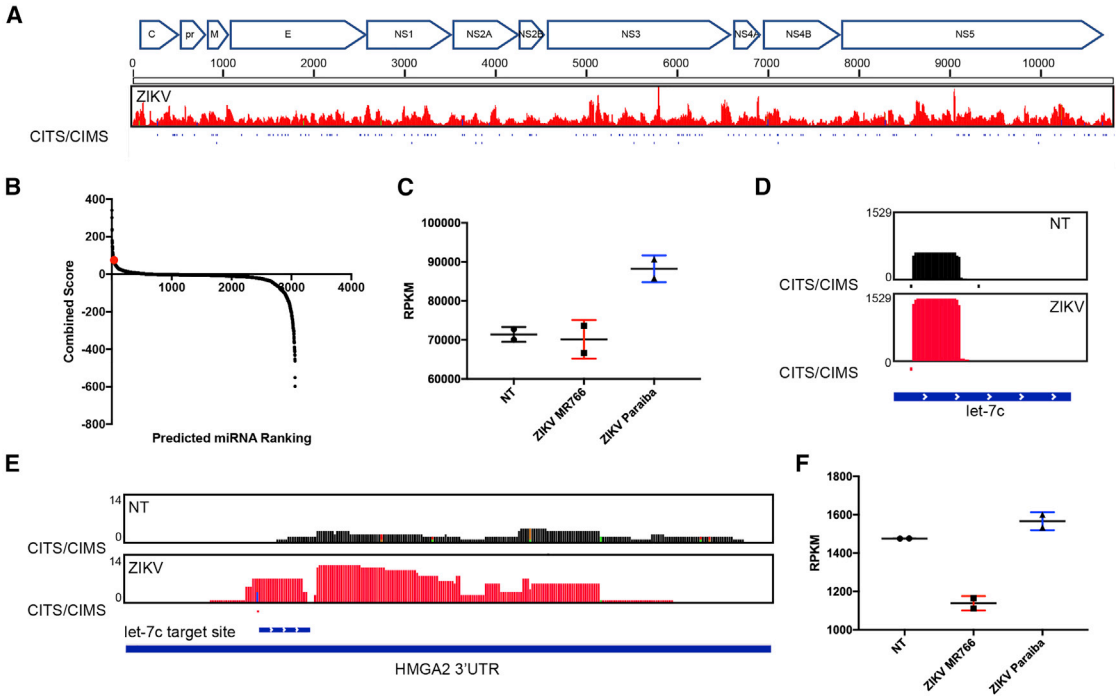

Figure 3. Zika Virus Upregulates let-7c and Represses *HMGA2*

(A) AGO binding map of the ZIKV Paraiba genome after infection of hNSCs at an MOI of 1 for 4 days. Crosslink-induced truncation or mutation sites (CITS/CIMS) that provide nucleotide resolution for AGO binding are shown as tick marks.

(B) Scatterplot showing the ranking and combined score of miRNAs predicted to regulate genes associated with microcephaly based on the Harmonizome database. *hsa-let-7c* (rank 36) is highlighted in red.

(C) miRNA-seq analysis of *let-7c* expression in mock-infected (NT), ZIKV MR766-infected, and Paraiba-infected hNSCs 2 days after infection at an MOI of 1. Scatterplot indicates mean and SD of n = 2 of biological replicates.

(D) AGO binding maps of mock-infected (NT) and Paraiba ZIKV-infected hNSCs 4 days post-infection at an MOI of 1 show significantly enriched loading of *let-7c* in the RISC after ZIKV infection.

(E) AGO binding maps of mock-infected (NT) and ZIKV-infected hNSCs show significantly enriched binding within the *HMGA2* 3′ UTR after ZIKV infection. The predicted let-7c target site is shown below the plots.

(F) RNA-seq analysis of *HMGA2* expression in mock-infected (NT), ZIKV MR766-infected, and Paraiba-infected hNSCs 2 days after infection at an MOI of 1. Scatterplot indicates mean and SD of n = 2 biological replicates.

See also Figure S3.

let-7c transcription and downregulation of its target genes, including the established regulator of NSC renewal, *HMGA2*.

The Harmonizome database analysis also predicted *miR-124-3p* to be involved in the ZIKV-induced microcephaly phenotype (Figure S4A). Similar to *let-7c*, this mRNA also shows a slight, although not statistically significant, upregulated expression (Figure S4B) but an increased association with AGO (Figure S4C) after ZIKV infection of hNSCs. Since no *miR-124-3p* targets with potential functions in neural stem cell biology or ZIKV pathogenesis have yet been identified, we looked for genes that were significantly downregulated by ZIKV Paraiba and MR766 infection of hNSCs and are also predicted target genes of *miR-124-3p* (Figure S4D). We selected the transferrin receptor (*TFRC*) from the 8 potential target genes identified—*FLRT3*, *LAMC1*, *NRCAM*, *TFRC*, *C3orf58*, *NRP1*, *TXNRD1*, and *RCAN1*—for further analysis, since it has known roles in stem cell self-renewal (Schonberg et al., 2015). Moreover, *TFRC* shows high species conservation of the putative *miR-124*-3p-binding site, suggesting that its regulation by *miR-124-3p* has an important function (Figures S4E and S4F). Notably, ZIKV infection of hNSCs resulted in increased AGO binding at the *TFRC* 3′ UTR and in a concomitant decrease in *TFRC* mRNA levels (Figures 4A and 4B).

We next sought to confirm the relevance of our findings *in vivo* using *Ifnar1*$^{-/-}$ mice. Six days after ZIKV infection, the mice were sacrificed, and the brains were removed, sectioned, and stained for ZIKVE and neuronal cell markers to identify infected cells. We found that the ZIKVE colocalized with the NSC marker SOX2 in the hippocampus and subventricular zone regions (Figures S4G and S4H), consistent with previous reports (Li et al., 2016a, 2016b) that ZIKV preferentially infects these cells. Moreover, qRT-PCR analysis of brain tissue confirmed that *TFRC* mRNA levels were downregulated in the infected, compared with uninfected, mice (Figure 4C). Thus, we have identified two miRNA-mRNA interactions that could contribute to the neurodegenerative phenotype induced by ZIKV infection.

Potential Role for *miR-124-3p–TFRC* Interactions in the Maintenance of NSCs *In Vivo*

To investigate the role of miR-124-3p and its putative target *TFRC* in ZIKV-mediated microcephaly, neurosphere growth kinetics

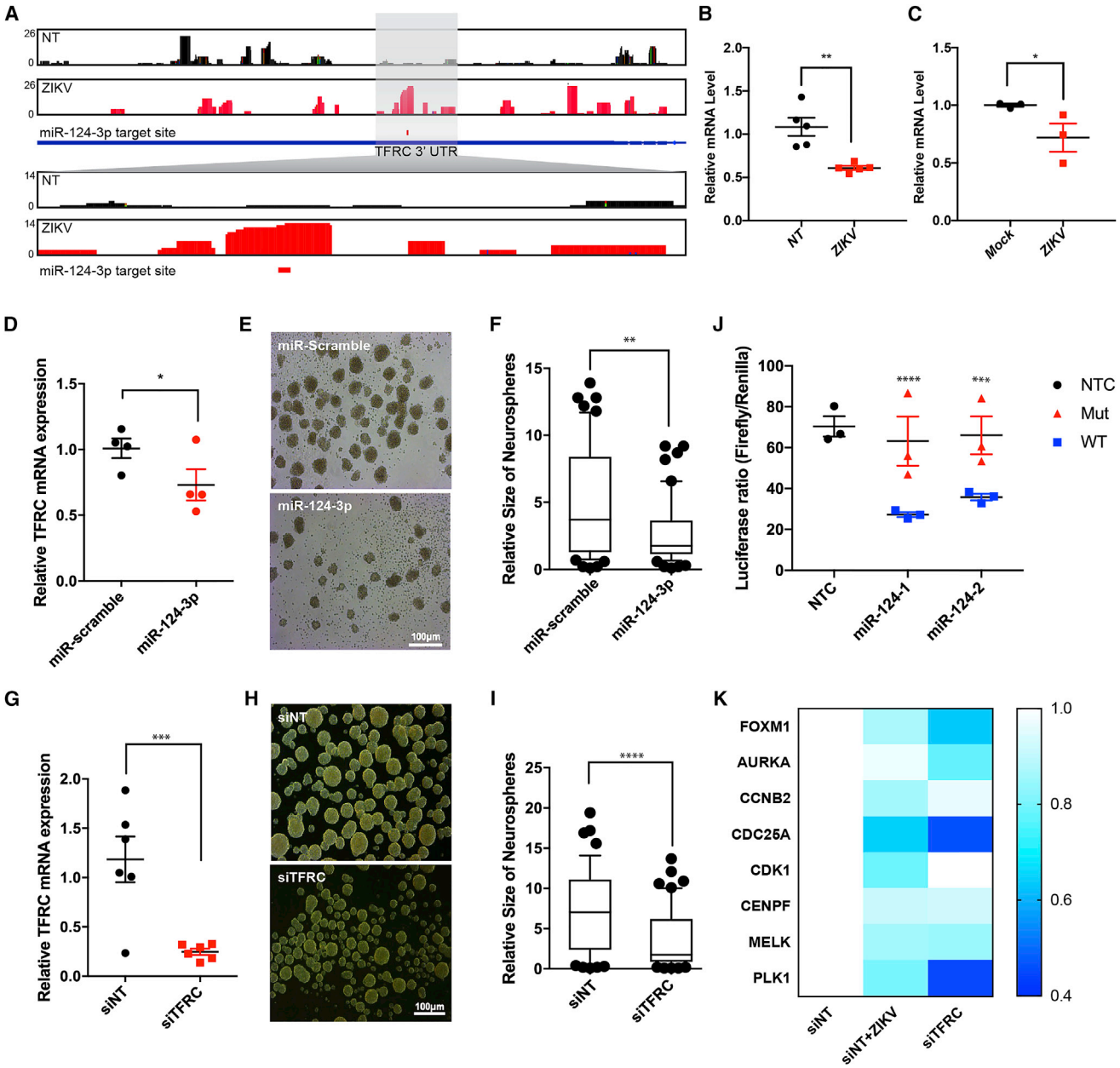

Figure 4. ZIKV Infection Modulates *miR-124-3p* and Its Target Gene *TFRC In Vitro* and *In Vivo*

(A) AGO binding maps of mock-infected (NT) and Paraiba ZIKV-infected hNSCs show significantly enriched binding within the *TFRC* 3′ UTR 4 days after ZIKV infection at an MOI of 1. The predicted *miR-124-3p* binding site is shown below.

(B) qRT-PCR analysis of *TFRC* mRNA levels in mock-infected (NT) and ZIKV Paraiba-infected hNSCs at 3 days post-infection at an MOI of 1. Data indicate means ± SEM of n = 5 biological replicates. **p < 0.01.

(C) qRT-PCR analysis of *Tfrc* mRNA levels in the brains of mock-infected and ZIKV Paraiba-infected *Ifnar*$^{-/-}$ 4- to 5-week-old adult mice at 6 days after infection. Data indicate means ± SEM of n = 3 biological replicates. *p < 0.05.

(D) qRT-PCR analysis of *TFRC* mRNA levels after overexpression of miRNA-124-3p mimic in hNSCs. Error bar represents the mean ± SEM of n = 4 biological replicates, *p < 0.05.

(E) Representative bright-field images of human neural stem cells (hNSC) derived neurospheres with scrambled control and miRNA-124-3p mimic overexpression. Scale bar represents 100 μm.

(F) Neurospheres show significant reduction in size after the overexpression of miR-124-3p mimic, as compared to the scrambled group, quantified by ImageJ. Box-and-whisker plots show mean and 25th and 75th percentiles. Error bars represent the 10th and 90th percentiles; n = 3. **p < 0.001, Student's t test.

(G) qRT-PCR analysis of *TFRC* mRNA levels after siRNA-mediated *TFRC* knockdown in hNSCs. Error bar represents the mean ± SEM of n = 6 biological replicates. ***p < 0.0001.

(legend continued on next page)

were evaluated (Dang et al., 2016; Tiwari et al., 2014b) following miR-124-3p overexpression and *TFRC* knockdown. miR-124 mimic overexpression downregulated *TFRC* mRNA level (Figure 4D) and reduced the size of neurospheres, as compared to scrambled miRNA transfected samples (Figures 4E and 4F). Similarly, knockdown of *TFRC* by small interfering RNA (siRNA) in hNSC-derived neurospheres resulted in attenuated neurosphere size, as compared to a scrambled control group, consistent with miR-124-3p overexpression (Figures 4G–4I).

Next, the direct interaction between miR-124-3p and *TFRC* was investigated, using a dual luciferase assay containing the TFRC 3′ UTR and miRNA seed sequence target site. To validate whether miR-124-3p targets TFRC through this putative miR-124-3p binding site in the 3′ UTR, we utilized a luciferase reporter construct (pGL3) in which the human TFRC 3′ UTR, containing either a wild-type (WT) or mutant miR-124-3p binding sequence, was placed immediately downstream of the luciferase gene. 293FT cells were co-transfected with WT or mutant type (Mut) reporter constructs with miR-124-3p mimics and pRLuc null plasmid expressing Renilla luciferase. Luciferase reporter activity of WT constructs was significantly reduced in cells co-transfected with miR-124-3p (Figure 4J). However, luciferase activity was not abolished in reporter constructs containing the mutant target sequence, indicating that miR-124-3p represses TFRC expression by specifically binding to the predicted target sites in the 3′ UTR of TFRC (Figure 4J).

To gain insight into the mechanism by which *TFRC* downregulation might affect NSCs, we examined the effects of siRNA-mediated *TFRC* knockdown in hNSCs on *TFRC* target genes involved in cell-cycle regulation. Several studies have shown that TFR plays a role in glioblastoma stem cell proliferation and self-renewal through the FOXM1 transcriptional regulatory signaling loop, which decreases the expression of cell-cycle genes (Schonberg et al., 2015; Silvestroff et al., 2013). Notably, we found that siRNA-mediated knockdown of *TFRC* or ZIKV infection decreased the expression of *FOXM1* as well as downstream targets of the FOXM1 regulatory axis—*AURKA*, *CCNB2*, *CDC25A*, *CDK1*, *CENPF*, *MELK*, and *PLK1*—which play important roles in cell-cycle regulation (Figure 4K).

Collectively, the results presented here shed light on the functional role of miRNAs, particularly *miR-124-3p*, in post-transcriptional regulation of ZIKV-infected hNSCs and the associated microcephaly phenotype.

DISCUSSION

In this study, we performed integrative analyses of coding and non-coding transcriptomes in hNSCs, which revealed miRNA-mRNA networks that may be dysregulated during ZIKV infection and may contribute to the microcephaly phenotype. Analysis of the dynamic transcriptomic landscape and RNAs bound to AGO following ZIKV infection revealed the dysregulation of genes associated with cell cycle, neurogenesis, stem cell maintenance, and metabolism. While previous studies have shown that ZIKV-induced perturbation of cell cycle, neurogenesis, and stem-cell-related processes contributes to the microcephaly phenotype, only a few mechanisms have been proposed to explain how ZIKV modulates these pathways (Dang et al., 2016; Gabriel et al., 2017; Hamel et al., 2015; Li et al., 2016a; Liang et al., 2016; Onorati et al., 2016; Tang et al., 2016). Our findings point to miRNA-mediated dysregulated gene expression as a potential contributing factor to the microcephaly phenotype.

One key finding from analysis of miRNA-mRNA networks in ZIKV-infected cells is that multiple differentially expressed miRNAs may potentially regulate the same mRNA targets implicated in microcephaly. For instance, *miR-125a-3p* and *miR-125a-5p*, which were upregulated by ZIKV infection, are both negative regulators of *MAVS*, an essential signaling protein in the RIG-I and type I interferon (IFN) response pathways of the innate immune system (Baril et al., 2009). *miR-320c* and *miR-7-5p*, also upregulated by ZIKV, target *SIN3A* mRNA, which encodes a STAT3-interacting repressor with an essential role in the IFN-mediated antiviral response (Icardi et al., 2012). Previous work showed that ZIKV inhibits type I IFN production through a mechanism involving ZIKV NS5 binding to STAT2 to promote its proteasomal degradation (Grant et al., 2016; Kumar et al., 2016). Thus, our findings reveal a potential mechanism by which miRNAs mediate suppression of IFN signaling in ZIKV-infected hNSCs and suggest that multiple miRNAs work in concert to suppress immunity- and neurodegeneration-related gene networks. Future work involving gain- and loss-of-function studies of specific miRNAs would further reveal the effects of ZIKV on proposed miRNA-mRNA networks.

Many of the miRNAs differentially expressed upon ZIKV infection showed enhanced binding to AGO. Using the Harmonizome database, we screened these for miRNAs and target genes with the potential ability to dysregulate neurogenesis and induce microcephaly. We confirmed an association between *let-7c* and *HMGA2* in hNSCs, as previously described (Nishino et al., 2008). Interestingly, *HMGA2* expression is also repressed in cells infected by human cytomegalovirus, which can also cause birth defects such as microcephaly (Shlapobersky et al., 2006).

In addition to *let-7c*, *hsa-miR-124-3p* was identified as a ZIKV-modulated miRNA with a potential role in microcephaly. miR-124-3p has also been shown to be upregulated in THP-1 cells latently infected with human cytomegalovirus (Fu et al.,

(H) Representative bright-field images of human-neural-stem-cell (hNSC)-derived neurospheres in scrambled control and transferrin receptor siRNA (siTFRC)-transfected groups. Scale bar represents 100 μm.
(I) Neurospheres show significant reduction in size after the knocking down of the TFRC gene, as compared to the scrambled group, quantified by ImageJ. Box-and-whisker plots show mean and 25th and 75th percentiles. Error bars represent the 10th and 90th percentiles; n = 3. **p < 0.001, Student's t test.
(J) HEK293T cells were transfected with luciferase reporter constructs containing WT or mutant (GTGCCTT to TGTATCG) TFRC 3′ UTRs. Firefly reporter luciferase activity was measured and normalized to Renilla activity. Error bar represents the mean ± SEM of n = 3 biological replicates; **p < 0.001, Student's t test.
(K) Heatmap of qRT-PCR analysis of target genes downstream of STA3-FOXM1 in hNSCs transfected with control siRNA (siNT) or *TFRC*-specific siRNA for 3 days or transfected with siNT and infected with ZIKV Paraiba for 3 days. Data indicate mean of n = 6 biological replicates. Color code shows the expression relative to that of the siNT samples.
See also Figure S4.

2014; Gérardin et al., 2018). The putative *miR-124-3p* target gene *TFRC* encodes the transferrin receptor TFR, which regulates cellular iron uptake and metabolism and plays a role in stem cell renewal and cell-cycle regulation (Sanchez et al., 2006; Schonberg et al., 2015; Silvestroff et al., 2013). In addition, TFRC1 has been shown to promote the proliferation of rat NSCs (Silvestroff et al., 2013). Interestingly, *TFRC* is highly upregulated in cancer stem cells and plays a role in glioblastoma stem cell renewal through an iron-dependent pathway involving the transcriptional regulators STAT3 and FOXM1 (Schonberg et al., 2015). Targeting of iron metabolic pathways can decrease cancer stem cell growth *in vitro* and *in vivo* (Schonberg et al., 2015). Moreover, iron negatively regulates replication of the flavivirus hepatitis C virus by binding to the Mg^{2+} binding pocket of the viral polymerase NS5B (Fillebeen and Pantopoulos, 2010; Fillebeen et al., 2005). Thus, there are multiple potential mechanisms by which miRNA-mediated downregulation of *TFRC* might dysregulate host metabolic processes and perturb the cell cycle during ZIKV infection.

Collectively, the data presented here identify miRNA-regulated transcriptional networks involved in self-renewal, cell-cycle progression, and neurogenesis in ZIKV-infected hNSCs, providing a possible mechanism by which the virus inflicts neuronal damage during brain development.

STAR★METHODS

Detailed methods are provided in the online version of this paper and include the following:

- KEY RESOURCES TABLE
- CONTACT FOR REAGENT AND RESOURCE SHARING
- EXPERIMENTAL MODEL AND SUBJECT DETAILS
  - Cell Lines and Culture Conditions
  - ZIKV Propagation
  - Ifnar −/− Mouse Handling
  - ZIKV Infection of Mice
- METHOD DETAILS
  - Plaque-Forming Assay
  - Immunofluorescence Microscopy
  - RNA-seq and miRNA-seq Library Preparation
  - RNA Extraction, cDNA Synthesis, and qRT-PCR
  - AGO-iCLIP-seq Library Preparation
  - RNA-Seq and miRNA-Seq Data Analysis
  - AGO-iCLIP-seq Bioinformatic Analysis
  - Transfection of miR-124-3p mimics and siTFRC gene in human NSC
  - miR-124-3p 3′UTR target Dual Glo Luciferase Assay
- QUANTIFICATION AND STATISTICAL ANALYSIS
- DATA AND SOFTWARE AVAILABILITY

SUPPLEMENTAL INFORMATION

Supplemental Information can be found online at https://doi.org/10.1016/j.celrep.2019.05.059.

ACKNOWLEDGMENTS

We thank Gene Yeo and Amy Pasquinelli for their advice on AGO-iCLIP experiments. We also thank Steve Head and the staff of the Next Generation Sequencing core facility at The Scripps Research Institute for help with the HT-seq and data analysis and members of the Rana lab for helpful discussions and advice. This work was supported in part by NIH grants to T.M.R. (CA177322, DP1DA039562, AI125103, and DA046171).

AUTHOR CONTRIBUTIONS

J.W.D. designed and performed experiments, analyzed the data, and wrote the manuscript; S.K.T. designed and performed experiments, analyzed the data, and participated in figure preparation; Y.Q. analyzed the data and participated in figure preparation; and T.M.R. contributed to the concept and design, data analysis and interpretation, and manuscript writing. All authors approved the final version of this manuscript.

DECLARATION OF INTERESTS

T.M.R. is a founder of ViRx Pharmaceuticals and a member of its scientific advisory board. The terms of this arrangement have been reviewed and approved by the University of California, San Diego, in accordance with its conflict of interest policies.

Received: May 15, 2017
Revised: January 16, 2019
Accepted: May 16, 2019
Published: June 18, 2019

REFERENCES

Agarwal, V., Bell, G.W., Nam, J.W., and Bartel, D.P. (2015). Predicting effective microRNA target sites in mammalian mRNAs. eLife *4*, e05005.

Ambros, V. (2004). The functions of animal microRNAs. Nature *431*, 350–355.

Baek, D., Villén, J., Shin, C., Camargo, F.D., Gygi, S.P., and Bartel, D.P. (2008). The impact of microRNAs on protein output. Nature *455*, 64–71.

Baril, M., Racine, M.E., Penin, F., and Lamarre, D. (2009). MAVS dimer is a crucial signaling component of innate immunity and the target of hepatitis C virus NS3/4A protease. J. Virol. *83*, 1299–1311.

Bartel, D.P. (2009). MicroRNAs: target recognition and regulatory functions. Cell *136*, 215–233.

Betel, D., Wilson, M., Gabow, A., Marks, D.S., and Sander, C. (2008). The microRNA.org resource: targets and expression. Nucleic Acids Res. *36*, D149–D153.

Bindea, G., Mlecnik, B., Hackl, H., Charoentong, P., Tosolini, M., Kirilovsky, A., Fridman, W.H., Pagès, F., Trajanoski, Z., and Galon, J. (2009). ClueGO: a Cytoscape plug-in to decipher functionally grouped gene ontology and pathway annotation networks. Bioinformatics *25*, 1091–1093.

Brasil, P., Sequeira, P.C., Freitas, A.D., Zogbi, H.E., Calvet, G.A., de Souza, R.V., Siqueira, A.M., de Mendonca, M.C., Nogueira, R.M., de Filippis, A.M., and Solomon, T. (2016). Guillain-Barré syndrome associated with Zika virus infection. Lancet *387*, 1482.

Büssing, I., Slack, F.J., and Grosshans, H. (2008). let-7 microRNAs in development, stem cells and cancer. Trends Mol. Med. *14*, 400–409.

Chi, S.W., Zang, J.B., Mele, A., and Darnell, R.B. (2009). Argonaute HITS-CLIP decodes microRNA-mRNA interaction maps. Nature *460*, 479–486.

Chou, C.H., Chang, N.W., Shrestha, S., Hsu, S.D., Lin, Y.L., Lee, W.H., Yang, C.D., Hong, H.C., Wei, T.Y., Tu, S.J., et al. (2016). miRTarBase 2016: updates to the experimentally validated miRNA-target interactions database. Nucleic Acids Res. *44* (*D1*), D239–D247.

Cloney, R. (2016). Non-coding RNA: deciphering the rules of microRNA targeting. Nat. Rev. Genet. *17*, 718.

Cugola, F.R., Fernandes, I.R., Russo, F.B., Freitas, B.C., Dias, J.L., Guimarães, K.P., Benazzato, C., Almeida, N., Pignatari, G.C., Romero, S., et al. (2016). The Brazilian Zika virus strain causes birth defects in experimental models. Nature *534*, 267–271.

Dang, J., Tiwari, S.K., Lichinchi, G., Qin, Y., Patil, V.S., Eroshkin, A.M., and Rana, T.M. (2016). Zika virus depletes neural progenitors in human cerebral organoids through activation of the innate immune receptor TLR3. Cell Stem Cell *19*, 258–265.

Davis, A.P., Grondin, C.J., Johnson, R.J., Sciaky, D., King, B.L., McMorran, R., Wiegers, J., Wiegers, T.C., and Mattingly, C.J. (2017). The Comparative Toxicogenomics Database: update 2017. Nucleic Acids Res. *45* (*D1*), D972–D978.

Dodt, M., Roehr, J.T., Ahmed, R., and Dieterich, C. (2012). FLEXBAR—flexible barcode and adapter processing for next-generation sequencing platforms. Biology (Basel) *1*, 895–905.

Eacker, S.M., Dawson, T.M., and Dawson, V.L. (2009). Understanding microRNAs in neurodegeneration. Nat. Rev. Neurosci. *10*, 837–841.

Fillebeen, C., and Pantopoulos, K. (2010). Iron inhibits replication of infectious hepatitis C virus in permissive Huh7.5.1 cells. J. Hepatol. *53*, 995–999.

Fillebeen, C., Rivas-Estilla, A.M., Bisaillon, M., Ponka, P., Muckenthaler, M., Hentze, M.W., Koromilas, A.E., and Pantopoulos, K. (2005). Iron inactivates the RNA polymerase NS5B and suppresses subgenomic replication of hepatitis C Virus. J. Biol. Chem. *280*, 9049–9057.

Fu, M., Gao, Y., Zhou, Q., Zhang, Q., Peng, Y., Tian, K., Wang, J., and Zheng, X. (2014). Human cytomegalovirus latent infection alters the expression of cellular and viral microRNA. Gene *536*, 272–278.

Gabriel, E., Ramani, A., Karow, U., Gottardo, M., Natarajan, K., Gooi, L.M., Goranci-Buzhala, G., Krut, O., Peters, F., Nikolic, M., et al. (2017). Recent Zika virus isolates induce premature differentiation of neural progenitors in human brain organoids. Cell Stem Cell *20*, 397–406.e5.

Gérardin, P., Ramos, R.C., Jungmann, P., de Oliveira, J.R.M., Amara, A., and Gressens, P. (2018). Zika epidemic: a step towards understanding the infectious causes of microcephaly? Lancet Infect. Dis. *18*, 15–16.

Grant, A., Ponia, S.S., Tripathi, S., Balasubramaniam, V., Miorin, L., Sourisseau, M., Schwarz, M.C., Sánchez-Seco, M.P., Evans, M.J., Best, S.M., and García-Sastre, A. (2016). Zika virus targets human STAT2 to inhibit type I interferon signaling. Cell Host Microbe *19*, 882–890.

Grimson, A., Farh, K.K., Johnston, W.K., Garrett-Engele, P., Lim, L.P., and Bartel, D.P. (2007). MicroRNA targeting specificity in mammals: determinants beyond seed pairing. Mol. Cell *27*, 91–105.

Grozhik, A.V., Linder, B., Olarerin-George, A.O., and Jaffrey, S.R. (2017). Mapping m^6A at individual-nucleotide resolution using crosslinking and immunoprecipitation (miCLIP). Methods Mol. Biol. *1562*, 55–78.

Haecker, I., Gay, L.A., Yang, Y., Hu, J., Morse, A.M., McIntyre, L.M., and Renne, R. (2012). Ago HITS-CLIP expands understanding of Kaposi's sarcoma-associated herpesvirus miRNA function in primary effusion lymphomas. PLoS Pathog. *8*, e1002884.

Hafner, M., Landthaler, M., Burger, L., Khorshid, M., Hausser, J., Berninger, P., Rothballer, A., Ascano, M., Jr., Jungkamp, A.C., Munschauer, M., et al. (2010). Transcriptome-wide identification of RNA-binding protein and microRNA target sites by PAR-CLIP. Cell *141*, 129–141.

Hamel, R., Dejarnac, O., Wichit, S., Ekchariyawat, P., Neyret, A., Luplertlop, N., Perera-Lecoin, M., Surasombatpattana, P., Talignani, L., Thomas, F., et al. (2015). Biology of Zika virus infection in human skin cells. J. Virol. *89*, 8880–8896.

Hu, G., Yao, H., Chaudhuri, A.D., Duan, M., Yelamanchili, S.V., Wen, H., Cheney, P.D., Fox, H.S., and Buch, S. (2012). Exosome-mediated shuttling of microRNA-29 regulates HIV Tat and morphine-mediated neuronal dysfunction. Cell Death Dis. *3*, e381.

Hu, B., Huo, Y., Yang, L., Chen, G., Luo, M., Yang, J., and Zhou, J. (2017). ZIKV infection effects changes in gene splicing, isoform composition and lncRNA expression in human neural progenitor cells. Virol. J. *14*, 217.

Huang, da W., Sherman, B.T., and Lempicki, R.A. (2009). Systematic and integrative analysis of large gene lists using DAVID bioinformatics resources. Nat. Protoc. *4*, 44–57.

Huppertz, I., Attig, J., D'Ambrogio, A., Easton, L.E., Sibley, C.R., Sugimoto, Y., Tajnik, M., König, J., and Ule, J. (2014). iCLIP: protein-RNA interactions at nucleotide resolution. Methods *65*, 274–287.

Icardi, L., Mori, R., Gesellchen, V., Eyckerman, S., De Cauwer, L., Verhelst, J., Vercauteren, K., Saelens, X., Meuleman, P., Leroux-Roels, G., et al. (2012). The Sin3a repressor complex is a master regulator of STAT transcriptional activity. Proc. Natl. Acad. Sci. USA *109*, 12058–12063.

König, J., Zarnack, K., Rot, G., Curk, T., Kayikci, M., Zupan, B., Turner, D.J., Luscombe, N.M., and Ule, J. (2010). iCLIP reveals the function of hnRNP particles in splicing at individual nucleotide resolution. Nat. Struct. Mol. Biol. *17*, 909–915.

Konig, J., Zarnack, K., Rot, G., Curk, T., Kayikci, M., Zupan, B., Turner, D.J., Luscombe, N.M., and Ule, J. (2011). iCLIP–transcriptome-wide mapping of protein-RNA interactions with individual nucleotide resolution. J. Vis. Exp. (*50*), 2638.

Kumar, A., Hou, S., Airo, A.M., Limonta, D., Mancinelli, V., Branton, W., Power, C., and Hobman, T.C. (2016). Zika virus inhibits type-I interferon production and downstream signaling. EMBO Rep. *17*, 1766–1775.

Kutmon, M., Kelder, T., Mandaviya, P., Evelo, C.T., and Coort, S.L. (2013). CyTargetLinker: a cytoscape app to integrate regulatory interactions in network analysis. PLoS ONE *8*, e82160.

Lanford, R.E., Hildebrandt-Eriksen, E.S., Petri, A., Persson, R., Lindow, M., Munk, M.E., Kauppinen, S., and Ørum, H. (2010). Therapeutic silencing of microRNA-122 in primates with chronic hepatitis C virus infection. Science *327*, 198–201.

Lawrence, M., Gentleman, R., and Carey, V. (2009). rtracklayer: an R package for interfacing with genome browsers. Bioinformatics *25*, 1841–1842.

Lazear, H.M., and Diamond, M.S. (2016). Zika virus: new clinical syndromes and its emergence in the Western Hemisphere. J. Virol. *90*, 4864–4875.

Lewis, B.P., Burge, C.B., and Bartel, D.P. (2005). Conserved seed pairing, often flanked by adenosines, indicates that thousands of human genes are microRNA targets. Cell *120*, 15–20.

Li, H., Handsaker, B., Wysoker, A., Fennell, T., Ruan, J., Homer, N., Marth, G., Abecasis, G., and Durbin, R.; 1000 Genome Project Data Processing Subgroup (2009). The Sequence Alignment/Map format and SAMtools. Bioinformatics *25*, 2078–2079.

Li, C., Xu, D., Ye, Q., Hong, S., Jiang, Y., Liu, X., Zhang, N., Shi, L., Qin, C.F., and Xu, Z. (2016a). Zika virus disrupts neural progenitor development and leads to microcephaly in mice. Cell Stem Cell *19*, 120–126.

Li, H., Saucedo-Cuevas, L., Regla-Nava, J.A., Chai, G., Sheets, N., Tang, W., Terskikh, A.V., Shresta, S., and Gleeson, J.G. (2016b). Zika virus infects neural progenitors in the adult mouse brain and alters proliferation. Cell Stem Cell *19*, 593–598.

Liang, Q., Luo, Z., Zeng, J., Chen, W., Foo, S.S., Lee, S.A., Ge, J., Wang, S., Goldman, S.A., Zlokovic, B.V., et al. (2016). Zika virus NS4A and NS4B proteins deregulate Akt-mTOR signaling in human fetal neural stem cells to inhibit neurogenesis and induce autophagy. Cell Stem Cell *19*, 663–671.

Liu, N., Landreh, M., Cao, K., Abe, M., Hendriks, G.J., Kennerdell, J.R., Zhu, Y., Wang, L.S., and Bonini, N.M. (2012). The microRNA miR-34 modulates ageing and neurodegeneration in Drosophila. Nature *482*, 519–523.

Love, M.I., Huber, W., and Anders, S. (2014). Moderated estimation of fold change and dispersion for RNA-seq data with DESeq2. Genome Biol. *15*, 550.

Melton, C., Judson, R.L., and Blelloch, R. (2010). Opposing microRNA families regulate self-renewal in mouse embryonic stem cells. Nature *463*, 621–626.

Nishino, J., Kim, I., Chada, K., and Morrison, S.J. (2008). Hmga2 promotes neural stem cell self-renewal in young but not old mice by reducing p16Ink4a and p19Arf Expression. Cell *135*, 227–239.

O'Connell, R.M., Rao, D.S., Chaudhuri, A.A., and Baltimore, D. (2010). Physiological and pathological roles for microRNAs in the immune system. Nat. Rev. Immunol. *10*, 111–122.

Onorati, M., Li, Z., Liu, F., Sousa, A.M.M., Nakagawa, N., Li, M., Dell'Anno, M.T., Gulden, F.O., Pochareddy, S., Tebbenkamp, A.T.N., et al. (2016). Zika virus disrupts phospho-TBK1 localization and mitosis in human neuroepithelial stem cells and radial glia. Cell Rep. *16*, 2576–2592.

Pasquinelli, A.E. (2012). MicroRNAs and their targets: recognition, regulation and an emerging reciprocal relationship. Nat. Rev. Genet. *13*, 271–282.

Rouillard, A.D., Gundersen, G.W., Fernandez, N.F., Wang, Z., Monteiro, C.D., McDermott, M.G., and Ma'ayan, A. (2016). The harmonizome: a collection of processed datasets gathered to serve and mine knowledge about genes and proteins. Database (Oxford) *2016*, baw100.

Sanchez, M., Galy, B., Dandekar, T., Bengert, P., Vainshtein, Y., Stolte, J., Muckenthaler, M.U., and Hentze, M.W. (2006). Iron regulation and the cell cycle: identification of an iron-responsive element in the 3′-untranslated region of human cell division cycle 14A mRNA by a refined microarray-based screening strategy. J. Biol. Chem. *281*, 22865–22874.

Sarno, M., Sacramento, G.A., Khouri, R., do Rosário, M.S., Costa, F., Archanjo, G., Santos, L.A., Nery, N., Jr., Vasilakis, N., Ko, A.I., and de Almeida, A.R. (2016). Zika virus infection and stillbirths: a case of hydrops fetalis, hydranencephaly and fetal demise. PLoS Negl. Trop. Dis. *10*, e0004517.

Schonberg, D.L., Miller, T.E., Wu, Q., Flavahan, W.A., Das, N.K., Hale, J.S., Hubert, C.G., Mack, S.C., Jarrar, A.M., Karl, R.T., et al. (2015). Preferential iron trafficking characterizes glioblastoma stem-like cells. Cancer Cell *28*, 441–455.

Selbach, M., Schwanhäusser, B., Thierfelder, N., Fang, Z., Khanin, R., and Rajewsky, N. (2008). Widespread changes in protein synthesis induced by microRNAs. Nature *455*, 58–63.

Shannon, P., Markiel, A., Ozier, O., Baliga, N.S., Wang, J.T., Ramage, D., Amin, N., Schwikowski, B., and Ideker, T. (2003). Cytoscape: a software environment for integrated models of biomolecular interaction networks. Genome Res. *13*, 2498–2504.

Shin, J., Shin, Y., Oh, S.M., Yang, H., Yu, W.J., Lee, J.P., Huh, S.O., Lee, S.H., Suh, Y.H., Chung, S., and Kim, H.S. (2014). MiR-29b controls fetal mouse neurogenesis by regulating ICAT-mediated Wnt/β-catenin signaling. Cell Death Dis. *5*, e1473.

Shlapobersky, M., Sanders, R., Clark, C., and Spector, D.H. (2006). Repression of HMGA2 gene expression by human cytomegalovirus involves the IE2 86-kilodalton protein and is necessary for efficient viral replication and inhibition of cyclin A transcription. J. Virol. *80*, 9951–9961.

Silvestroff, L., Franco, P.G., and Pasquini, J.M. (2013). Neural and oligodendrocyte progenitor cells: transferrin effects on cell proliferation. ASN Neuro *5*, e00107.

Simonin, Y., Loustalot, F., Desmetz, C., Foulongne, V., Constant, O., Fournier-Wirth, C., Leon, F., Molès, J.P., Goubaud, A., Lemaitre, J.M., et al. (2016). Zika virus strains potentially display different infectious profiles in human neural cells. EBioMedicine *12*, 161–169.

Sullivan, C.S., and Ganem, D. (2005). MicroRNAs and viral infection. Mol. Cell *20*, 3–7.

Taganov, K.D., Boldin, M.P., Chang, K.J., and Baltimore, D. (2006). NF-kappaB-dependent induction of microRNA miR-146, an inhibitor targeted to signaling proteins of innate immune responses. Proc. Natl. Acad. Sci. USA *103*, 12481–12486.

Tang, H., Hammack, C., Ogden, S.C., Wen, Z., Qian, X., Li, Y., Yao, B., Shin, J., Zhang, F., Lee, E.M., et al. (2016). Zika virus infects human cortical neural progenitors and attenuates their growth. Cell Stem Cell *18*, 587–590.

Tiwari, M., Sharma, L.K., Vanegas, D., Callaway, D.A., Bai, Y., Lechleiter, J.D., and Herman, B. (2014a). A nonapoptotic role for CASP2/caspase 2: modulation of autophagy. Autophagy *10*, 1054–1070.

Tiwari, S.K., Agarwal, S., Seth, B., Yadav, A., Nair, S., Bhatnagar, P., Karmakar, M., Kumari, M., Chauhan, L.K., Patel, D.K., et al. (2014b). Curcumin-loaded nanoparticles potently induce adult neurogenesis and reverse cognitive deficits in Alzheimer's disease model via canonical Wnt/β-catenin pathway. ACS Nano *8*, 76–103.

Trapnell, C., Pachter, L., and Salzberg, S.L. (2009). TopHat: discovering splice junctions with RNA-Seq. Bioinformatics *25*, 1105–1111.

Wang, X.H., Aliyari, R., Li, W.X., Li, H.W., Kim, K., Carthew, R., Atkinson, P., and Ding, S.W. (2006). RNA interference directs innate immunity against viruses in adult Drosophila. Science *312*, 452–454.

Webb, S., Hector, R.D., Kudla, G., and Granneman, S. (2014). PAR-CLIP data indicate that Nrd1-Nab3-dependent transcription termination regulates expression of hundreds of protein coding genes in yeast. Genome Biol. *15*, R8.

Wu, Y.E., Parikshak, N.N., Belgard, T.G., and Geschwind, D.H. (2016). Genome-wide, integrative analysis implicates microRNA dysregulation in autism spectrum disorder. Nat. Neurosci. *19*, 1463–1476.

Yu, K.R., Shin, J.H., Kim, J.J., Koog, M.G., Lee, J.Y., Choi, S.W., Kim, H.S., Seo, Y., Lee, S., Shin, T.H., et al. (2015). Rapid and efficient direct conversion of human adult somatic cells into neural stem cells by HMGA2/let-7b. Cell Rep. *10*, 441–452.

Zhu, L.J., Gazin, C., Lawson, N.D., Pagès, H., Lin, S.M., Lapointe, D.S., and Green, M.R. (2010). ChIPpeakAnno: a Bioconductor package to annotate ChIP-seq and ChIP-chip data. BMC Bioinformatics *11*, 237.

STAR★METHODS

KEY RESOURCES TABLE

REAGENT or RESOURCE	SOURCE	IDENTIFIER
Antibodies		
mouse anti-ZIKVE/anti-flavivirus group antigen	Millipore	Cat# MAB10216, RRID:AB_827205
rabbit anti-SOX2	Abcam	Cat# AB97959, RRID:AB_2341193
rabbit anti-NeuN	Millipore	Cat# ABN78, RRID:AB_10807945
AGO 2A8 antibody	Millipore	Cat# MABE56, RRID:AB_11214388
Bacterial and Virus Strains		
ZIKV prototype MR766	National Institutes of Health	LC002520.1
ZIKV Brazilian strain Paraiba	Stevenson Laboratory, University of Miami Life Science and Technology Park	KX280026.1
Chemicals, Peptides, and Recombinant Proteins		
StemPro Neural Supplement	ThermoFisher	A1050901
Eagle's Minimum Essential Medium	ATCC	30-2003
RNase I	Ambion	AM2295
RNA phenol/chloroform	Ambion	9722
^{32}P-γ-ATP	Perkin Elmer	blu002250uc
Critical Commercial Assays		
iScript One-Step RT-PCR kit	Bio-Rad	1708892
NEBNext Ultra II Directional RNA Library Kit for Illumina	NEB	E7760L
Q5 master mix	NEB	M0494S
miRNeasy Mini Kit	QIAGEN	217004
iScript Mastermix	Bio-Rad	1708891
SYBR Green PCR Master Mix	Bio-Rad	1725270
protein A/G Dynabeads	ThermoFisher	88802
4-12% NuPAGE Bis-Tris gels	Invitrogen	NP0321BOX
Superscript III reverse transcriptase	Invitrogen	18080093
precast 6% Tris/Borate/EDTA-urea gels	Invitrogen	EC6265BOX
Circligase II	Epicenter	CL9021K
Deposited Data		
Raw and processed data	GEO	GSE113640
Raw and processed RNA-seq data	GEO	GSE113636
Raw and processed AGO-iCLIP-seq data	GEO	GSE113638
Raw and processed miRNA-seq data	GEO	GSE113639
Experimental Models: Cell Lines		
Human neural stem cells	ThermoFisher	A15654
Vero	ATCC	CCL-81
Experimental Models: Organisms/Strains		
B6.129S2-Ifnar1tm1Agt/Mmjax	MMRC Jackson Laboratories	32045-JAX
Oligonucleotides		
RT-qPCR ZIKV-F: TTGGTCATGATACTGCTGATTGC	IDT	N/A
RT-qPCR ZIKV-R: CCCTCCACGAAGTCTCTATTGC	IDT	N/A

(*Continued on next page*)

Continued

REAGENT or RESOURCE	SOURCE	IDENTIFIER
L3 linker (HPLC-purified): /5rApp/AGATCGGAAGAGCG GTTCAG/3ddC/	IDT	N/A
Cut oligo (PAGE-purified): GTTCAGGATCCACGACGCT CTTC/3ddC/	IDT	N/A
P5 Solexa PCR primer: AATGATACGGCGACCACCGA GATCTACACTCTTTCCCTACACGACGCTC TTCCGATCT	IDT	N/A
P3 Solexa PCR primer: CAAGCAGAAGACGGCATACG AGATCGGTCTCGGCATTCCTGCTGAAC CGCTCTTCCGATCT	IDT	N/A
RT1: /5phos/NnaaccNNNAGATCGGAAGAGCGTCGT GgatcCTGAACCGC	IDT	N/A
RT2: /5phos/NNacaaNNNAGATCGGAAGAGCGTCGT GgatcCTGAACCGC	IDT	N/A
RT3: /5phos/NNattgNNNAGATCGGAAGAGCGTCGT GgatcCTGAACCGC	IDT	N/A
RT4: /5phos/NNaggtNNNAGATCGGAAGAGCGTCGT GgatcCTGAACCGC	IDT	N/A
RT5: /5phos/NNcgccNNNAGATCGGAAGAGCGTCGT GgatcCTGAACCGC	IDT	N/A
RT6: /5phos/NNccggNNNAGATCGGAAGAGCGTCGT GgatcCTGAACCGC	IDT	N/A
Software and Algorithms		
TopHat v 1.4.1	(Trapnell et al., 2009)	https://ccb.jhu.edu/software/tophat/index.shtml
PRINSEQ v 0.20.3		http://prinseq.sourceforge.net
SAMtools	(Li et al., 2009)	http://samtools.sourceforge.net
DESeq2	(Love et al., 2014)	https://bioconductor.org/packages/release/bioc/html/DESeq2.html
Partek		http://www.partek.com
The Database for Annotation, Visualization and Integrated Discovery (DAVID)	(Huang et al., 2009)	https://david.ncifcrf.gov
Cytoscape	(Shannon et al., 2003)	https://cytoscape.org
TargetScan	(Agarwal et al., 2015)	http://www.targetscan.org/vert_72/
miRTarBase	(Chou et al., 2016)	http://mirtarbase.mbc.nctu.edu.tw/php/index.php
miRANDA	(Betel et al., 2008)	http://cbio.mskcc.org/microrna_data/manual.html
pyCRAC	(Webb et al., 2014)	http://sandergranneman.bio.ed.ac.uk/pyCRAC_software
flexbar	(Dodt et al., 2012)	https://github.com/seqan/flexbar/wiki/Manual
Novocraft		http://www.novocraft.com
ChIPpeakAnno	(Zhu et al., 2010)	https://bioconductor.org/packages/release/bioc/html/ChIPpeakAnno.html
rtracklayer	(Lawrence et al., 2009)	https://www.bioconductor.org/packages/release/bioc/html/rtracklayer.html
Supermatcher		http://emboss.sourceforge.net/apps/release/6.6/emboss/apps/supermatcher.html
GraphPad Prism		https://www.graphpad.com

CONTACT FOR REAGENT AND RESOURCE SHARING

Further information and requests for resources and reagents should be directed to the Lead Contact, Tariq Rana (trana@ucsd.edu).

EXPERIMENTAL MODEL AND SUBJECT DETAILS

Cell Lines and Culture Conditions

All cells were maintained at 37°C in a humidified 5% CO_2 atmosphere. Vero cells were maintained in Eagle's Minimum Essential Medium (EMEM; ATCC, 30-2003) supplemented with 10% fetal bovine serum (FBS; GIBCO) and antibiotics. Human NSCs (ThermoFisher, A15654) were cultured in StemPro NSC SFM medium consisting of Knockout DMEM/F-12 media supplemented with 2 mM GlutaMax, 20 ng/ml basic fibroblast growth factor, 20 ng/ml epidermal growth factor, and 2% StemPro Neural Supplement (ThermoFisher, A1050901) on Matrigel- or CELLStart-coated plates following the manufacturer's instructions.

ZIKV Propagation

ZIKV prototype MR766 (National Institutes of Health, LC002520.1) and Brazilian strain Paraiba (Stevenson Laboratory, University of Miami Life Science and Technology Park, KX280026.1) were propagated in the low passage Vero cell line. Vero cells were infected with virus at an MOI of 1 in EMEM medium supplemented with 10% FBS. The medium was refreshed 4 h after infection and the viral supernatant was collected at 5 days post-infection. Viral titers were assessed using iScript One-Step RT-PCR kit (Bio-Rad). Viral copy numbers were calculated from a standard curve of *in vitro*-transcribed viral RNA transcripts.

Ifnar −/− Mouse Handling

All studies were conducted in accordance with protocols approved by the Institutional Review Board of the University of California, San Diego. All animal work was performed in accordance with the guidelines of the Institutional Animal Care and Use Committee of the University of California, San Diego.

Ifnar$^{-/-}$ mice 4–5 weeks old were purchased from MMRRC Jackson Laboratories and housed according to regulatory standards approved by the Institutional Review Board of the University of California, San Diego.

ZIKV Infection of Mice

All studies were conducted in accordance with protocols approved by the Institutional Review Board of the University of California, San Diego. All animal work was performed in accordance with the guidelines of the Institutional Animal Care and Use Committee of the University of California, San Diego.

Ifnar$^{-/-}$ mice (4–5 weeks old; MMRRC Jackson Laboratories) were infected by intraperitoneal injection of 2.5×10^7 genome equivalents ZIKV Paraiba (500 μL of viral stock with 5×10^4 genome equivalents/μl) or 1.6×10^8 MR766 (500 μL of viral stock with 3.2×10^5 genome equivalents/μl). Mice were sacrificed at 6 days post-infection and brains were collected for RNA extraction and/or immunostaining (described above).

METHOD DETAILS

Plaque-Forming Assay

Vero cells were seeded in 12-well plates and incubated at 37°C in a 5% CO_2 incubator until they reached ~90%–100% confluency (~3 days). Cells were infected with serial 10-fold dilutions of ZIKV for 4–6 h and then overlaid with 4% agarose and incubated for 4 days. Cells were then fixed with 4% formaldehyde and stained with 0.1% crystal violet solution in 20% ethanol. Plaques were visualized under a microscope and counted. Plaque-forming units (PFU) were calculated as ([number of plaques × ZIKV dilution]) / infection volume) and are expressed as PFU/ml.

Immunofluorescence Microscopy

To assess ZIKV infection, hNSCs were fixed at 24, 48, and 72 h post-infection and immunostained as described previously (Dang et al., 2016). In brief, ZIKV- and mock-infected hNSCs were fixed with 4% paraformaldehyde (PFA) in phosphate-buffered saline (PBS) for 20 min at room temperature. Cells were permeabilized by incubation in 0.1% Triton X-100 for 5 min at room temperature and then blocked in 5% bovine serum albumin for 30 min. Cells were then incubated overnight at 4°C with a mouse anti-ZIKVE/anti-flavivirus group antigen (1:500, Millipore MAB10216), which is directed against the flavivirus envelope protein. Cells were washed with PBS and incubated for 1 h at room temperature with fluorescein isothiocyanate (FITC)-conjugated anti-mouse IgG. The nuclei were stained with Hoechst 33258 before analysis. Immunostained cells were imaged using a Leica fluorescence microscope (DMI 3000B).

For staining of brain sections, at the end of the experiment, mice were transcardially perfused with normal saline (0.9% NaCl) followed by ice-cold 4% PFA (pH 7.2) under deep anesthesia, as described previously (Tiwari et al., 2014a). Brains were removed and post-fixed in 10% PFA overnight at 4°C followed by cryopreservation in 10%, 20%, and 30% (w/v) sucrose in PBS. Serial coronal sections of 30 μm thickness were cut using a freezing cryostat (Leica Biosystems, CM3050s) beginning at the bregma −1.50 to −3.50 mm through the dorsal hippocampus encompassing the dentate gyrus region and +0.26 to −2.5 mm through the SVZ. Free-floating sections were washed, antigen retrieval was performed with citrate buffer (pH 6.2), and the sections were blocked with 3% normal goat serum, 0.1% Triton X-100, and 0.5% bovine serum albumin for 2 h. Sections were then incubated with mouse anti-ZIKVE antibody (1:500), rabbit anti-SOX2, or rabbit anti-NeuN (1:100) for 24 h at 4°C. Sections were then stained

with secondary antibodies (anti-mouse and anti-rabbit Alexa Fluor 488 at 1:200; anti-rabbit, anti-mouse, and anti-goat Alexa Fluor 594 at 1:200), washed, mounted with DAPI-containing Hard Set Anti-Fade mounting medium (Vectashield, Vector Laboratories, CA, USA), and stored in the dark at 4°C. Slides were analyzed using an inverted Leica fluorescence microscope (DMI 3000B) or a Leica SP5 confocal with Resonant Scanner microscope with Leica LAS Lite Software.

RNA-seq and miRNA-seq Library Preparation

RNA-seq libraries were generated using the NEBNext Ultra II Directional RNA Library Kit for Illumina (NEB, E7760L) according to the manufacturer's instructions. miRNA-seq libraries were generated by ligating Truseq 3′ and 5′ adapters using T4 RNA Ligase2 and T4 RNA Ligase, respectively. RNAs were reverse transcribed using Superscript II Reverse Transcriptase and PCR amplified using Q5 master mix (NEB M0494S). Sample quality was assessed using a high-sensitivity bioanalyzer.

RNA Extraction, cDNA Synthesis, and qRT-PCR

Total RNA was extracted from hNSCs using a miRNeasy Mini Kit (QIAGEN, 217004) according to the manufacturer's instructions. RNA samples were treated with RNase-free DNase (QIAGEN), and cDNA was generated from 500 ng RNA/sample using iScript Mastermix (Bio-Rad) according to the manufacturer's instructions. qPCR was performed with SYBR Green PCR Master Mix (Bio-Rad) using a Roche LightCycler 480 using ZIKV-specific forward (TTGGTCATGATACTGCTGATTGC) and reverse (CCCTCCACGAA GTCTCTATTGC) primers.

AGO-iCLIP-seq Library Preparation

AGO-iCLIP-seq libraries were prepared according to previously published methods (Huppertz et al., 2014; Konig et al., 2011). Briefly, hNSCs were infected with ZIKV Paraiba at an MOI of 1 and UV crosslinked with 150 mJ/cm^2 at 254 nm on ice. Cell pellets were harvested and lysed (50 mM Tris-HCl, pH 7.4, 100 mM NaCl, 1% NP-40, 0.1% SDS, 0.5% sodium deoxycholate, 1/100 protease inhibitor cocktail III, Calbiochem). RNAs were partially digested using RNase I (Ambion, AM2295) and Turbo DNase. Digested RNAs were incubated with washed protein A/G Dynabeads (Thermo Scientific, 88802) and 10 μg AGO 2A8 antibody (Millipore, Mill-MABE56) on a rotator overnight at 4°C. RNAs were immunoprecipitated and washed twice with a high-salt buffer (50 mM Tris-HCl, pH 7.4, 1 M NaCl. 1 mM EDTA, 1% NP-40, 0.1% SDS, 0.5% sodium deoxycholate) and twice with a wash buffer (20 mM Tris-HCl, pH 7.4, 10 mM $MgCl_2$, 0.2% Tween-20).

To prepare CLIP-seq libraries, 3′ ends of immunoprecipitated RNAs were dephosphorylated using PNK (Promega) for 20 min and then washed with high-salt buffer and twice with wash buffer (composition as above). Pre-adenylated L3 linkers were ligated to RNAs on resuspended beads using RNA ligase (NEB) at 16°C overnight in a thermocycler. RNAs were washed sequentially with wash buffer, high-salt buffer twice, and wash buffer to remove excess linker and enzyme. The 5′ ends were radiolabeled using ^{32}P-γ-ATP (Perkin Elmer, blu002250uc) and PNK.

Samples resolved by SDS-PAGE using 4%–12% NuPAGE Bis-Tris gels (Invitrogen) using 1 s MOPS running buffer following the manufacturer's instructions. RNA-protein complexes were transferred to nitrocellulose membranes and RNAs were released by proteinase K treatment and urea elution of the membranes. RNAs were recovered with RNA phenol/chloroform (Ambion, 9722) using Phase Lock Gel Heavy tubes and precipitated overnight with sodium acetate and ethanol.

Precipitated RNAs were reverse transcribed using Superscript III reverse transcriptase (Invitrogen) and indexing primers. cDNAs were gel purified using precast 6% Tris/Borate/EDTA-urea gels (Invitrogen) according to the manufacturer's instructions. Following gel purification, cDNAs were circularized using Circligase II (Epicenter) and linearized with BamHI (NEB). Linearized cDNAs were precipitated, PCR amplified using P5/P3 Solexa primers, and sequenced.

RNA-Seq and miRNA-Seq Data Analysis

RNA was extracted from hNSCs as described above and then ribo-depleted. RNA and miRNA sequencing were performed using an Illumina NextSeq 500 with an average of 20 million and 5 million reads per sample, respectively.

For RNA-seq analyses, the single-end reads that passed Illumina filters were filtered for reads aligning to tRNA, rRNA, adaptor sequences, and spike-in controls. The reads were then aligned to UCSC hg19 reference genome using TopHat (v 1.4.1). DUST scores were calculated with PRINSEQ Lite (v 0.20.3), and low-complexity reads (DUST > 4) were removed from the BAM files. The alignment results were parsed using SAMtools to generate SAM files. Read counts to each genomic feature were obtained with the htseq-count program (v 0.6.0) using the "union" option. After removing absent features (zero counts in all samples), the raw counts were imported into R/Bioconductor package DESeq2 to identify genes differentially expressed between samples. DESeq2 normalizes counts by dividing each column of the count table (samples) by the size factor of the column. The size factor was calculated by dividing the samples by the geometric means of the genes. This brought the count values to a common scale suitable for comparison. P values for differential expression were calculated using a binomial test for differences between the base means of two conditions. The p values were adjusted for multiple test correction using the Benjamini–Hochberg algorithm to control the false discovery rate. Cluster analyses, including principal component analysis and hierarchical clustering, were performed using standard algorithms and metrics.

For miRNA-seq analyses, quality control was assessed using FastQC. Reads were aligned to the genome with bowtie2 using the following reference and annotations: Homo_sapiens.GRCh38.dna.primary_assembly.fa (NCBI) and Homo_sapiens.GRCh38.86.gtf

(NCBI). Random 100 unmapped reads were generated and compared using BLAST (NCBI). Partek was used to generate read counts, RPKM, and the mapping summary. Genes with read count values < 1 across all samples were filtered out. DESeq2 was used to calculate the fold change, p value, and adjusted p value for differentially expressed miRNAs.

Gene ontology analyses of biological processes were performed using The Database for Annotation, Visualization and Integrated Discovery (DAVID) (Huang et al., 2009). Grouped functional pathway/gene ontology network and miR–mRNA target analyses were performed using Cytoscape with the ClueGo and CyTargetLinker add-ons (Bindea et al., 2009; Kutmon et al., 2013; Shannon et al., 2003). miRNA target predictions were performed using TargetScan, miRTarBase, and miRANDA (Agarwal et al., 2015; Betel et al., 2008; Chou et al., 2016; Kutmon et al., 2013). Density and cumulative density plots were generated in R after calculating the cumulative context scores of a given mRNA based on miRNA target sites within the 3′-UTR (Wu et al., 2016).

AGO-iCLIP-seq Bioinformatic Analysis

Peak calling was performed following previously established protocols (Grozhik et al., 2017) with some modifications. First, 3′ adapters were trimmed using flexbar (Dodt et al., 2012) and demultiplexed using pyCRAC (Webb et al., 2014). Control and infected samples were aggregated into separate files and subsampled for equal number of reads before proceeding. PCR duplicates were collapsed with pyCRAC and concatenated reads were aligned to hg38 or ZIKV kx280026.1 genome using Novocraft. To identify CIMS (crosslink-induced mutation sites), separate bed files were generated containing mutation coordinates and read coordinates by CTK-1.0.3. The CIMS algorithm was used to call mutation sites. CITS (crosslink-induced truncation sites) were identified using only forward reads.

To identify differential iCLIP-seq peaks, CITS and CIMS sites were combined for the two infected and control samples and DESeq2 was performed to determine statistically significant CITS/CIMS sites. Gene symbols were added using ChIPpeakAnno (Zhu et al., 2010), TxDb.Hsapiens.UCSC.hg38.knownGene, and rtracklayer (Lawrence et al., 2009). From the differential sites, FASTA sequences were generated using bedtools2-2.26.0 and analyzed for miRNA seed sequences using Supermatcher. The accession number for the AGO-iCLIP-seq data reported in this paper is GEO: GSE113640.

Transfection of miR-124-3p mimics and siTFRC gene in human NSC

hsa-miR-124-3p oligonucleotide mimics (sequence: UAAGGCACGCGGUGAAUGCC), scrambled control (sequence: UCACAACC UCCUAGAAAGAGUAGA), and siRNA for TFRC were obtained from Dharmacon (USA). hNSC were seeded in 12-well Matrigel coated plates at the density of 1 × 106 cells/well approximately 24h before transfection. hNSC were transfected with miRNA mimic, siTFRC or scrambled controls in antibiotic free Opti-MEM medium with final concentration of 50nM of miRNA mimic and 25nM of siTFRC for 48h. RNA was extracted to assess transfection efficiency and knockdown. The size of neurospheres was measured by ImageJ in control, miRNA mimic and siTFRC transfected groups.

miR-124-3p 3′UTR target Dual Glo Luciferase Assay

To verify the direct regulation of *TFRC* expression by miR-124-3p, dual glo luciferase assay was performed as described earlier (Hu et al., 2012; Shin et al., 2014). Briefly, the 3′UTR of human TFRC gene (ENST00000540528.1) was cloned into a pGL3 vector backbone (miTarget miRNA 3′-UTR target clones) obtained from GeneWiz (USA). The mutant construct was created by substituting TGTATCG for the WT sequence GTGCCTT within the miR-124-3p binding site in the 3′-UTR. For the reporter assay, 293FT cells were cultured for 24h in 24-well culture plate, followed by co-transfection of wild-type (WT) or mutant (MT) reporter constructs (50ng/well), pGL3-Promoter vector, miR-124-3p oligonucleotide (25nM/well) and pRLuc null plasmid expressing Renilla Luciferase (200ng/well) with lipofectamine-2000. Renilla luciferase activity was used as transfection normalization control for the miR-124-3p 3′UTR TFRC luciferase assay. After 48hr of transfection, cells were collected, and luciferase activity was measured by dual-luciferase reporter assay (Promega, Madison, WI, USA) as per manufacturer's instructions. The firefly luciferase activity was normalized by Renilla luciferase activity for each transfected well.

QUANTIFICATION AND STATISTICAL ANALYSIS

Statistical analysis was carried out using GraphPad Prism software. Differences between group means were analyzed by Student's t test. Statistical details regarding individual experiments can be found in the figure legends section. Differentially expressed genes in the RNA-seq data were analyzed using DESeq2. A adjusted p value $\leq$ 0.05 was considered statistically significant.

DATA AND SOFTWARE AVAILABILITY

Raw and processed data are provided in the Gene Expression Omnibus (accession number GSE113640; subseries GSE113636 for RNA-seq, GSE113638 for iCLIP-seq, and GSE113639 for miRNA-seq).

Cell Reports, Volume *27*

Supplemental Information

Genome-wide Integrative Analysis of Zika-Virus-Infected Neuronal Stem Cells Reveals Roles for MicroRNAs in Cell Cycle and Stemness

Jason W. Dang, Shashi Kant Tiwari, Yue Qin, and Tariq M. Rana

Figure S1

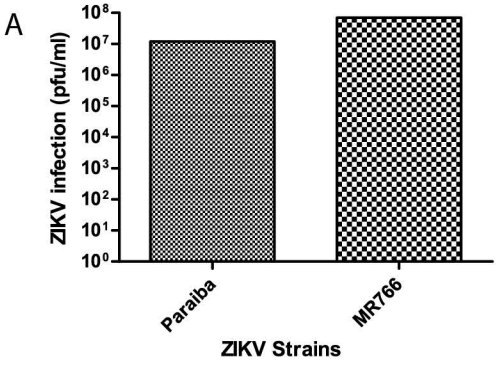
A
ZIKV infection (pfu/ml)
10^8
10^7
10^6
10^5
10^4
10^3
10^2
10^1
10^0
Paraiba
MR766
ZIKV Strains

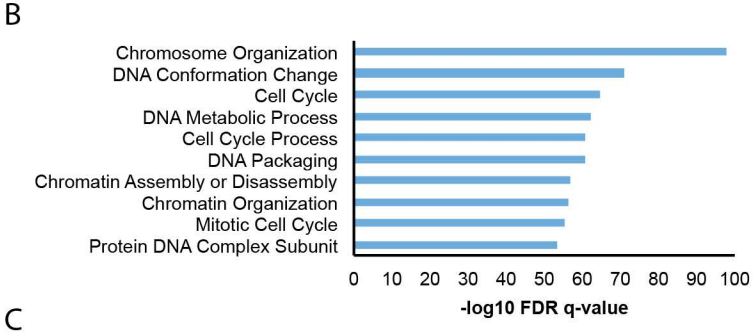
B
Chromosome Organization
DNA Conformation Change
Cell Cycle
DNA Metabolic Process
Cell Cycle Process
DNA Packaging
Chromatin Assembly or Disassembly
Chromatin Organization
Mitotic Cell Cycle
Protein DNA Complex Subunit
0 10 20 30 40 50 60 70 80 90 100
-log10 FDR q-value

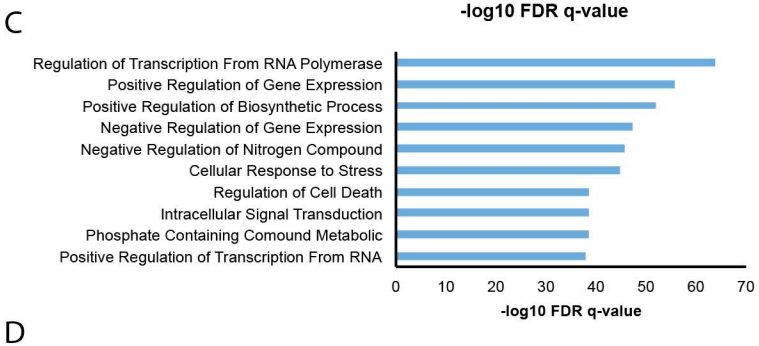
C
Regulation of Transcription From RNA Polymerase
Positive Regulation of Gene Expression
Positive Regulation of Biosynthetic Process
Negative Regulation of Gene Expression
Negative Regulation of Nitrogen Compound
Cellular Response to Stress
Regulation of Cell Death
Intracellular Signal Transduction
Phosphate Containing Comound Metabolic
Positive Regulation of Transcription From RNA
0 10 20 30 40 50 60 70
-log10 FDR q-value

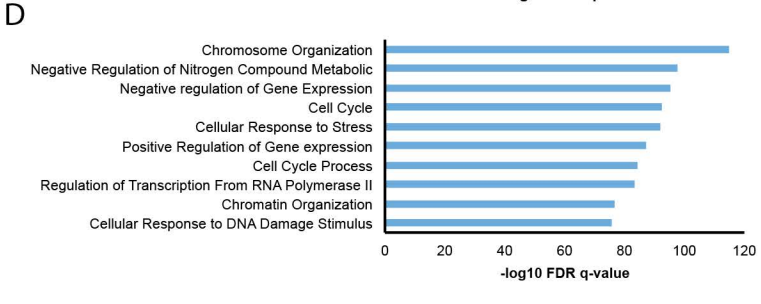
D
Chromosome Organization
Negative Regulation of Nitrogen Compound Metabolic
Negative regulation of Gene Expression
Cell Cycle
Cellular Response to Stress
Positive Regulation of Gene expression
Cell Cycle Process
Regulation of Transcription From RNA Polymerase II
Chromatin Organization
Cellular Response to DNA Damage Stimulus
0 20 40 60 80 100 120
-log10 FDR q-value

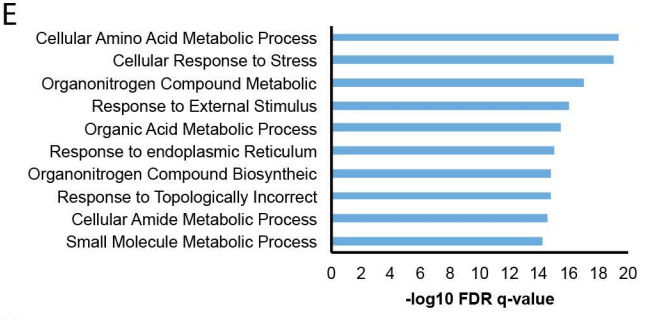
E
Cellular Amino Acid Metabolic Process
Cellular Response to Stress
Organonitrogen Compound Metabolic
Response to External Stimulus
Organic Acid Metabolic Process
Response to endoplasmic Reticulum
Organonitrogen Compound Biosyntheic
Response to Topologically Incorrect
Cellular Amide Metabolic Process
Small Molecule Metabolic Process
0 2 4 6 8 10 12 14 16 18 20
-log10 FDR q-value

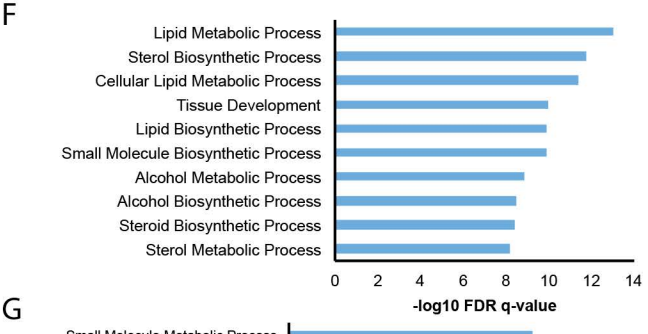
F
Lipid Metabolic Process
Sterol Biosynthetic Process
Cellular Lipid Metabolic Process
Tissue Development
Lipid Biosynthetic Process
Small Molecule Biosynthetic Process
Alcohol Metabolic Process
Alcohol Biosynthetic Process
Steroid Biosynthetic Process
Sterol Metabolic Process
0 2 4 6 8 10 12 14
-log10 FDR q-value

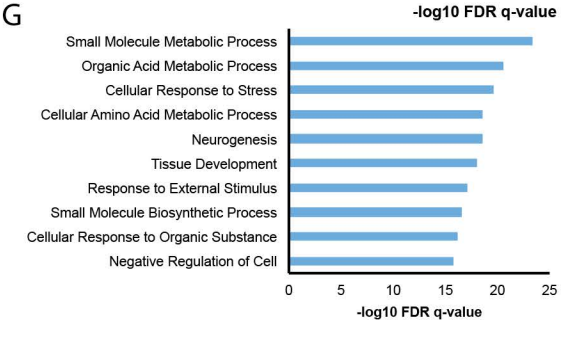
G
Small Molecule Metabolic Process
Organic Acid Metabolic Process
Cellular Response to Stress
Cellular Amino Acid Metabolic Process
Neurogenesis
Tissue Development
Response to External Stimulus
Small Molecule Biosynthetic Process
Cellular Response to Organic Substance
Negative Regulation of Cell
0 5 10 15 20 25
-log10 FDR q-value

Figure S1. Gene Set Enrichment Analyses of Differentially Expressed Genes in ZIKV-Infected hNSCs. Related to Figure 1.

(A) Plaque-forming assay measuring infectious particles of ZIKV Paraiba and MR766 strains. n=3 biological replicates.

(B–D) GSEA of upregulated (B), downregulated (C) or upregulated or downregulated (D) genes in ZIKV MR766-infected hNSCs at 3 days post-infection at a MOI of 1.

(E–G) As in (B–D) for ZIKV Paraiba-infected hNSCs.

Figure S2

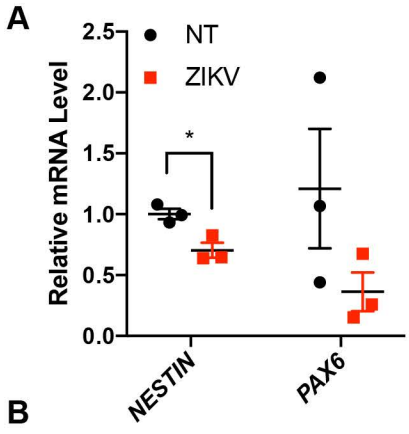
A
NT
ZIKV
Relative mRNA Level
2.5
2.0
1.5
1.0
0.5
0.0
*
NESTIN
PAX6

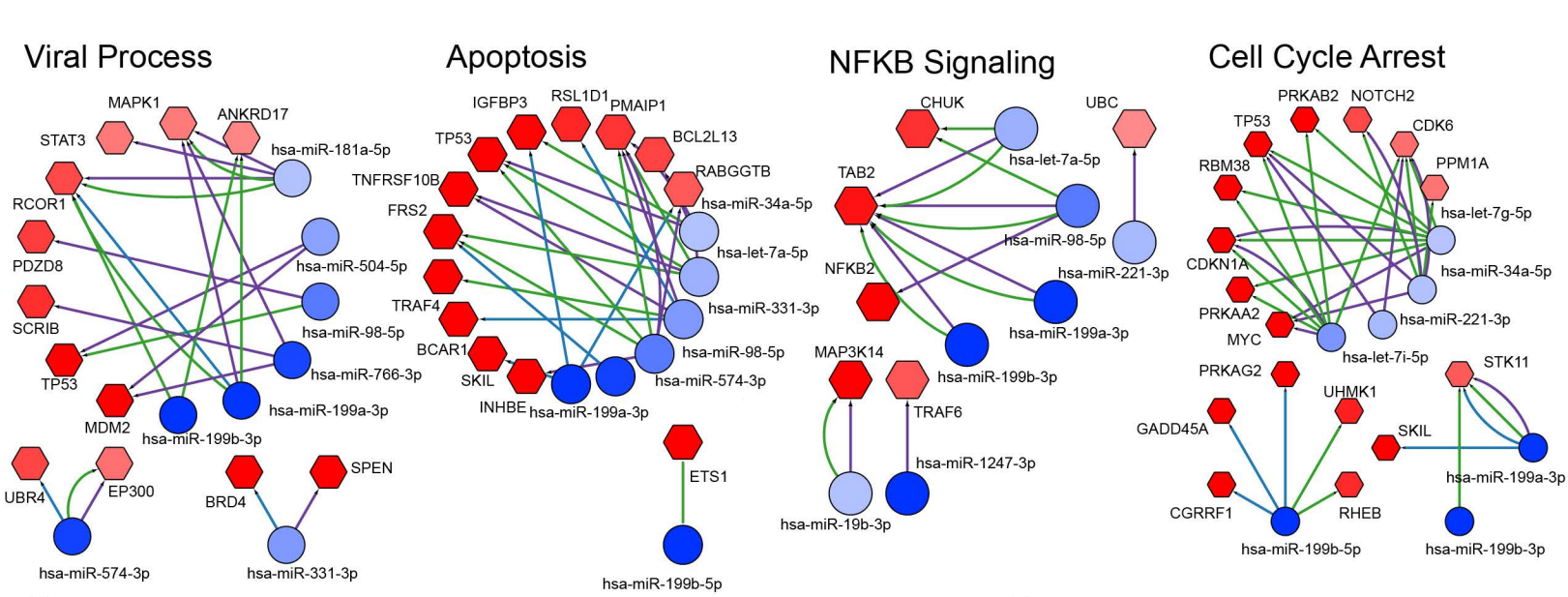
B
Viral Process
MAPK1
ANKRD17
STAT3
hsa-miR-181a-5p
RCOR1
PDZD8
hsa-miR-504-5p
SCRIB
hsa-miR-98-5p
TP53
hsa-miR-766-3p
MDM2
hsa-miR-199a-3p
hsa-miR-199b-3p
UBR4
EP300
BRD4
SPEN
hsa-miR-574-3p
hsa-miR-331-3p
Apoptosis
IGFBP3
RSL1D1
PMAIP1
TP53
BCL2L13
TNFRSF10B
RABGGTB
hsa-miR-34a-5p
FRS2
hsa-let-7a-5p
hsa-miR-331-3p
TRAF4
BCAR1
hsa-miR-98-5p
SKIL
hsa-miR-574-3p
INHBE
hsa-miR-199a-3p
ETS1
hsa-miR-199b-5p
NFKB Signaling
CHUK
UBC
hsa-let-7a-5p
TAB2
hsa-miR-98-5p
hsa-miR-221-3p
NFKB2
hsa-miR-199a-3p
MAP3K14
hsa-miR-199b-3p
TRAF6
hsa-miR-1247-3p
hsa-miR-19b-3p
Cell Cycle Arrest
PRKAB2
NOTCH2
TP53
CDK6
RBM38
PPM1A
hsa-let-7g-5p
CDKN1A
hsa-miR-34a-5p
PRKAA2
hsa-miR-221-3p
MYC
hsa-let-7i-5p
PRKAG2
STK11
UHMK1
GADD45A
SKIL
hsa-miR-199a-3p
CGRRF1
RHEB
hsa-miR-199b-5p
hsa-miR-199b-3p

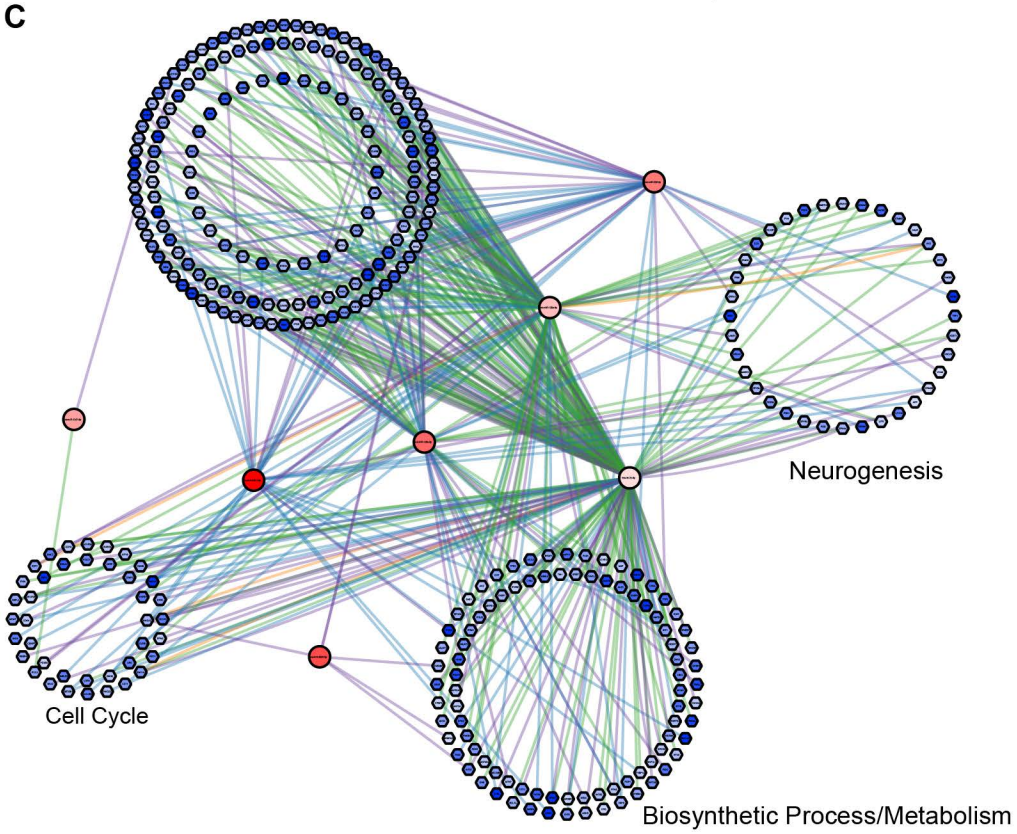
C
Neurogenesis
Cell Cycle
Biosynthetic Process/Metabolism

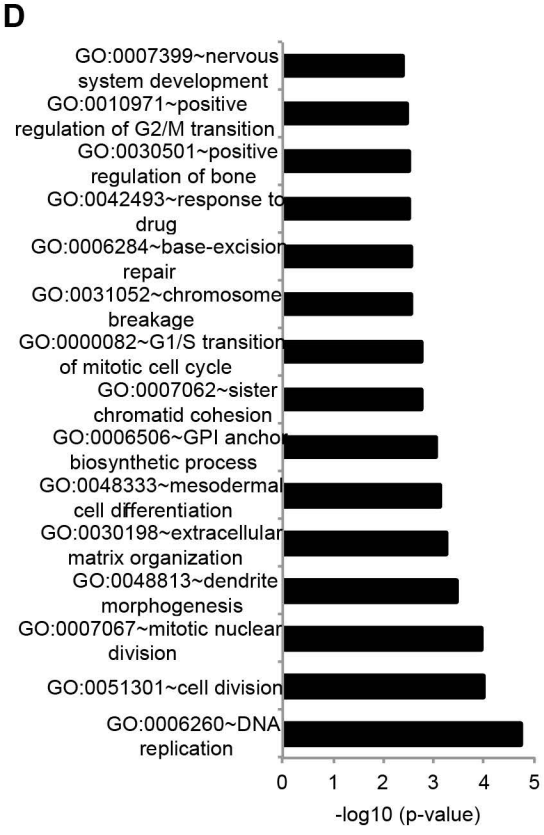
D
GO:0007399~nervous system development
GO:0010971~positive regulation of G2/M transition
GO:0030501~positive regulation of bone
GO:0042493~response to drug
GO:0006284~base-excision repair
GO:0031052~chromosome breakage
GO:0000082~G1/S transition of mitotic cell cycle
GO:0007062~sister chromatid cohesion
GO:0006506~GPI anchor biosynthetic process
GO:0048333~mesodermal cell differentiation
GO:0030198~extracellular matrix organization
GO:0048813~dendrite morphogenesis
GO:0007067~mitotic nuclear division
GO:0051301~cell division
GO:0006260~DNA replication
0
1
2
3
4
5
-log10 (p-value)

Figure S2. miRNA-Mediated Regulatory Networks in ZIKV-Infected hNSCs. Related to Figure 2.

(A) RT-qPCR analysis of *NESTIN* and *PAX6* mRNA levels in hNSCs 3 days post-infection with ZIKV MR766 or Paraiba at a MOI of 1. Mean ± SEM of n = 3 biological replicates. * $p < 0.05$.

(B) Integrative networks of mRNAs downregulated and miRNAs upregulated in ZIKV-infected hNSCs involved in "viral process," "apoptosis," "NFκB signaling," and "cell cycle arrest" based on gene ontology annotation.

(C) miRNA–mRNA network of commonly upregulated miRNAs and downregulated mRNAs in ZIKV MR766- and Paraiba-infected hNSCs. Genes are clustered based on gene ontology annotation.

(D) Gene ontology analyses of putative mRNA targets of commonly upregulated miRNAs in ZIKV MR766- and Paraiba-infected hNSCs (shown in Figure 2A-B).

Figure S3

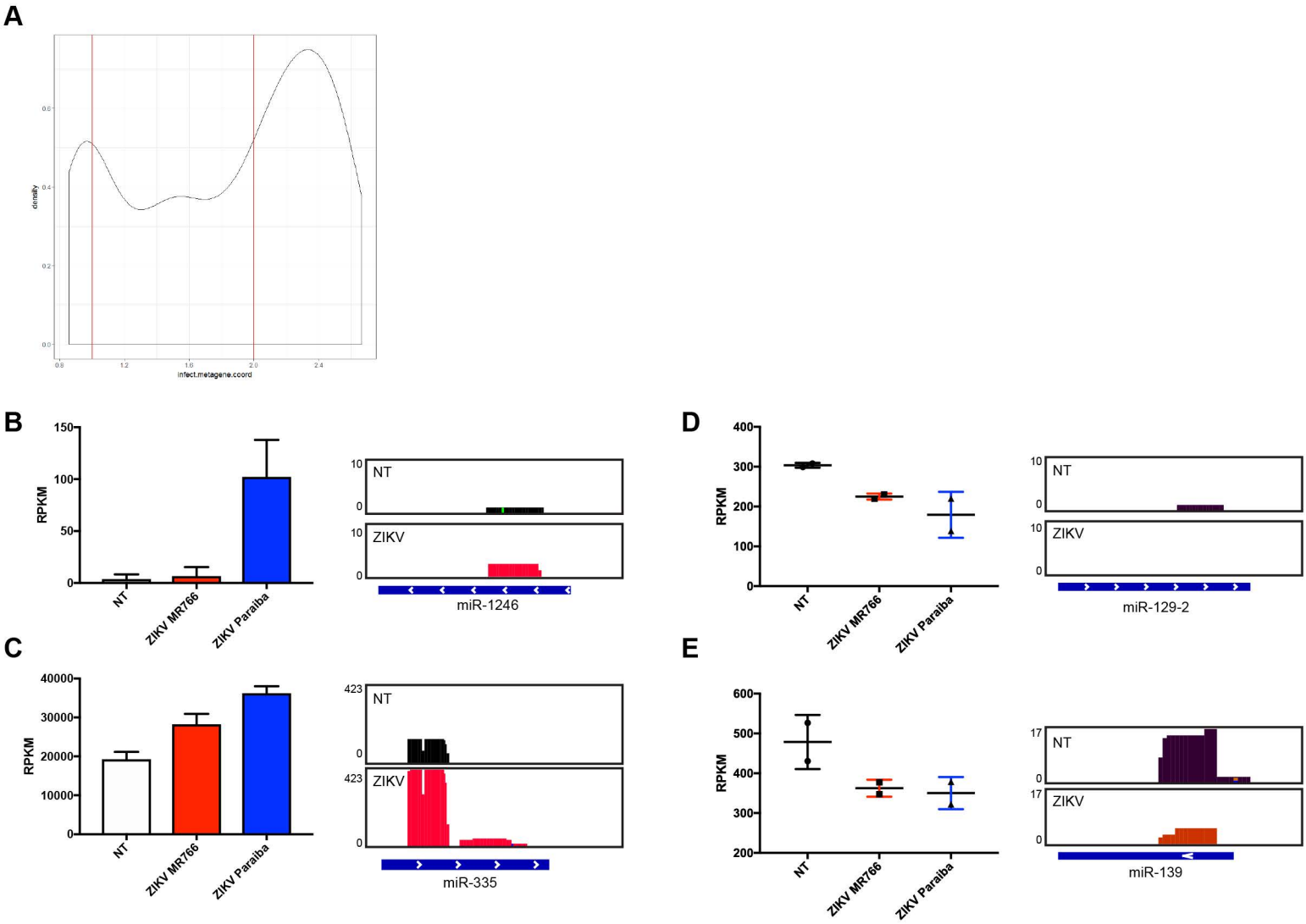
A
density
infect.metagene.coord
B
RPKM
NT
ZIKV MR766
ZIKV Paraiba
NT
ZIKV
miR-1246
C
RPKM
NT
ZIKV MR766
ZIKV Paraiba
NT
ZIKV
miR-335
D
RPKM
NT
ZIKV MR766
ZIKV Paraiba
NT
ZIKV
miR-129-2
E
RPKM
NT
ZIKV MR766
ZIKV Paraiba
NT
ZIKV
miR-139

Figure S3. Related to Figure 3.

(A) Metagene analysis of AGO-iCLIP-seq binding sites in ZIKV Paraiba infected hNSCs 4 days post-infect at MOI 1 shows enrichment in 3′-UTRs.

(B and C) miRNA-seq analysis in ZIKV MR766 and Paraiba infected hNSCs 3 days post-infect at MOI 1 (left) and AGO binding maps (right) in ZIKV Paraiba infected hNSCs 4 days post-infect at MOI 1show upregulation and enhanced binding of *miR-1246* (B) and *miR-335* (C).

(D and E) miRNA-seq analysis in ZIKV MR766 and Paraiba infected hNSCs 3 days post-infect at MOI 1 (left) and AGO binding maps in ZIKV Paraiba infected hNSCs 4 days post-infect at MOI 1 (right) show downregulation and decreased binding of *miR-129-2* (D) and *miR-139* (E).

Figure S4

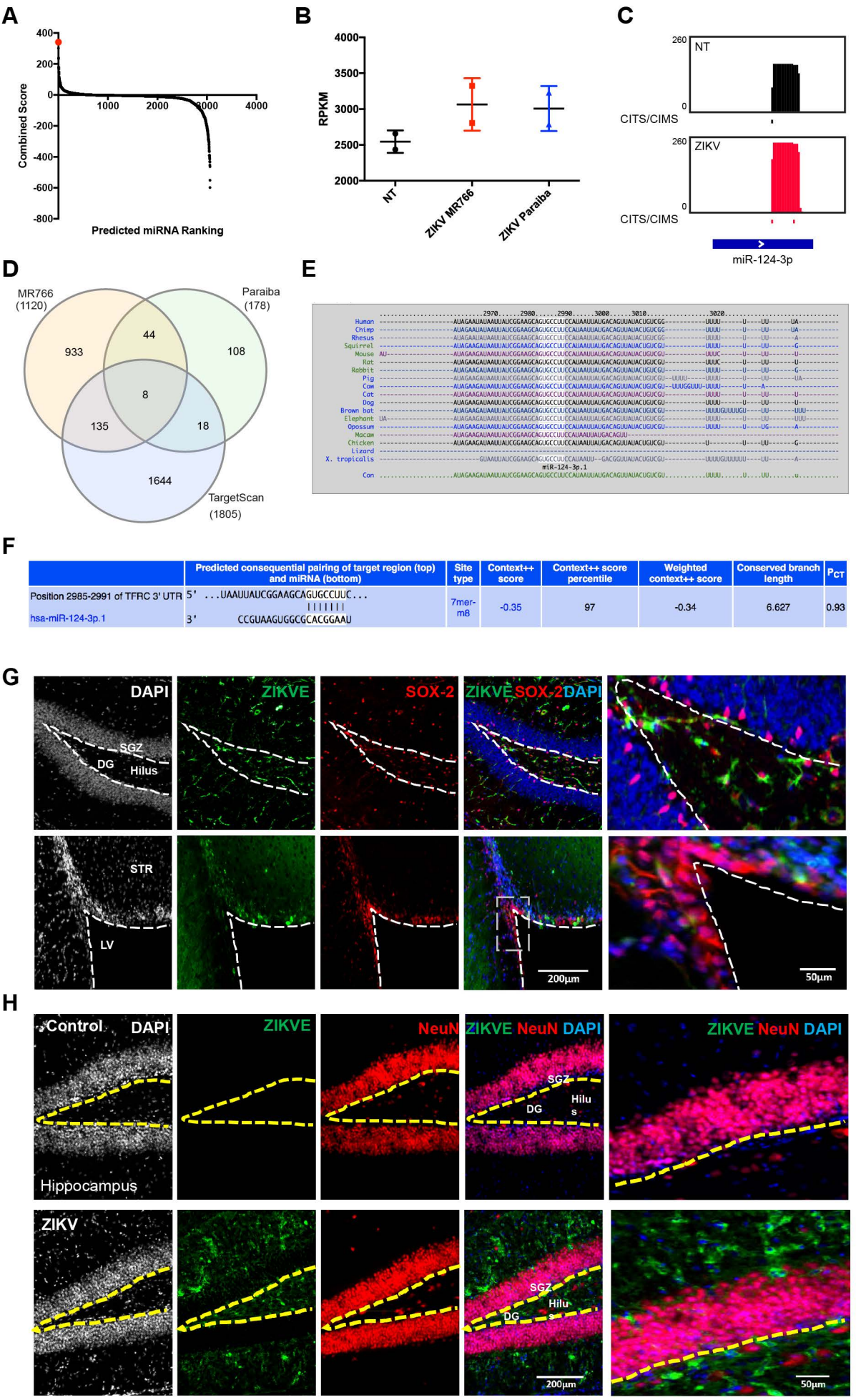
A
Combined Score
Predicted miRNA Ranking
B
RPKM
NT
ZIKV MR766
ZIKV Paraiba
C
NT
CITS/CIMS
ZIKV
CITS/CIMS
miR-124-3p
D
MR766 (1120)
Paraiba (178)
TargetScan (1805)
933
44
108
8
135
18
1644
E
Human
Chimp
Rhesus
Squirrel
Mouse
Rat
Rabbit
Pig
Cow
Cat
Dog
Brown bat
Elephant
Opossum
Macaw
Chicken
lizard
X. tropicalis
miR-124-3p.1
Con
F
Predicted consequential pairing of target region (top) and miRNA (bottom)
Site type
Context++ score
Context++ score percentile
Weighted context++ score
Conserved branch length
PCT
Position 2985-2991 of TFRC 3' UTR
5' ...UAAUUAUCGGAAGCAGUGCCUUC...
3' CCGUAAGUGGCGCACGGAAU
hsa-miR-124-3p.1
7mer-m8
-0.35
97
-0.34
6.627
0.93
G
DAPI
SGZ
DG
Hilus
ZIKVE
SOX-2
ZIKVE SOX-2 DAPI
STR
LV
200µm
50µm
H
Control
DAPI
Hippocampus
ZIKVE
NeuN
ZIKVE NeuN DAPI
SGZ
DG
Hilus
ZIKV
200µm
50µm

Figure S4. Related to Figure 4.

(A) Scatterplot showing the ranking and combined score of miRNAs predicted to regulate genes associated with microcephaly based on the Harmonizome databased. *hsa-miR-124-3p* (rank 1) is highlighted in red.

(B) miRNA-seq analysis in ZIKV MR766 and Paraiba infected hNSCs 3 days post-infect at MOI 1 show *miR-124-3p* expression following viral infection. Scatterplot mean and standard deviation of n=2 biological replicates.

(C) AGO binding maps of mock-infected (NT) and Paraiba ZIKV-infected hNSCs show significantly enriched loading of *miR-124-3p* in the RISC 4 days after ZIKV infection at MOI 1.

(D) Venn diagram of putative *miR-124-3p* target mRNAs (TargetScan) and significantly ($p < 0.05$) downregulated genes in ZIKV MR766- and Paraiba-infected hNSCs.

(E) Sequence conservation of putative *miR-124-3p*-binding site within *TFRC*.

(F) TargetScan prediction of the *miR-124-3p* targeting site within the *TFRC* 3′-UTR.

(G) Immunostaining of ZIKV envelope flavivirus group antigen (ZIKVE, green) and neural progenitor marker SOX2 (red) in the hippocampus (top row) and subventricular zone (bottom row) of a ZIKV Paraiba-infected *Ifnar*$^{-/-}$ mouse brain 6 days post-infection. Nuclei were stained with DAPI (gray or blue). Right-most column shows enlargement of the merged panels. SGZ = subgranular zone, DG = dentate gyrus, LV = lateral ventricle, STR = striatum. Scale bars, 200 μM and 50 μM. Dashed lines indicate separation between subgranular zone and dentate gyrus and hillus (top panels) and striatum and lateral ventricle (bottom panels).

(H) Immunostaining of ZIKV envelope antigen (ZIKV, green) and the mature neuronal marker NeuN (red) in the hippocampus of uninfected (top) or ZIKV Paraiba-infected (bottom) *Ifnar*$^{-/-}$ mice 6 days post-infection. Labeling and scale bars are as for (D). Dashed lines indicate separation between subgranular zone and dentate gyrus and hillus regions.